CrossMark

A nonlinear cohesive/friction coupled model for shear induced delamination of adhesive composite joint

P. F. Liu · Z. P. Gu · X. Q. Peng

Abstract This paper originally proposes a nonlinear cohesive/frictional contact coupled model for the mode-II shear delamination of adhesive composite joint based on a modified Xu and Needleman's exponential cohesive model. First, the friction is assumed to increase nonlinearly at the delamination interface when the tangential cohesive softening appears. Second, a non-associative plasticity model based on the Mohr–Coulomb frictional contact law is proposed, which includes a frictional slip criterion and a slip potential function. Third, a return mapping algorithm based on the non-associative plasticity theory is proposed to solve the updated normal and tangential tractions and stiffnesses. It is shown the tangential cohesive traction and stiffness depend on the friction and dilatancy of the delamination interface. Finally, the proposed theoretical model is implemented using three-dimensional finite element analysis by ABAQUS-UEL (user element subroutine) and demonstrated by comparing the finite element results with the analytical results for the $[0°]_6$, $[\pm30°]_5$, $[\pm45°]_5$ end-notched flexure adhesive composite joints with the mode-II shear delamination. The effects of the friction coefficient, cohesive strength, normal contact stiffness and mesh size on the load–displacement curves and delamination mechanisms of composites are studied. Numerical results show the shear delamination growth is governed by the transition from the decreased tangential cohesive traction to the increased tangential friction, and the frictional effect becomes distinct after unstable delamination for angle-ply laminates.

Keywords Cohesive/friction coupling · Adhesive composite joint · Mode-II shear delamination · Finite element analysis (FEA)

P. F. Liu (✉) · Z. P. Gu
Institute of Chemical Machinery and Process Equipment,
Zhejiang University, Hangzhou 310027, China
e-mail: pfliu@zju.edu.cn; 56691747@qq.com

P. F. Liu
State Key Laboratory of Strength and Vibration of
Mechanical Structures, Xi'an 710049, China

X. Q. Peng
School of Materials Science and Engineering, Shanghai Jiaotong
University, Shanghai 200030, China

1 Introduction

Fiber reinforced laminated composites have been increasingly used in fields of aerospace and aircraft due to high stiffness and strength as well as low density. An important work in the process of design and manufacture of lightweight composite structures is to seek efficient and robust jointing techniques between different components with similar or dissimilar material properties. Adhesive joining is one of the most favorable joining techniques in composites because they can

🙂 Springer

reduce detrimental stress concentration and guarantee structural integrity compared with traditional fasteners such as riveting and bolting, in which fiber cutting and interruption often result in severely non-uniform stress distributions (Mortensen and Thomsen 2002; Liljedahl et al. 2006; Gustafson and Waas 2009). Typical adhesive joint types include the single-lap joint, the double-lap joint, the strapped joint and the scarf joint (Noorman 2014).

Delamination between the adherend and the finite-thickness adhesive layer due to low bonding strength of the adhesive layer often leads to the loss of stiffness and strength of composite structures. Delamination issue of composites is essentially represented by the crack initiation and propagation. Interlaminar normal and tangential stresses between the adhesive/adherend interface increase, leading to the delamination failure of joints. From the fracture mechanics perspective, delamination occurs when the interlaminar crack resistance is exceeded by the energy release rate (ERR) (Mi et al. 1998; Xie and Waas 2006). From the micromechanical point of view, the ductile failure of pressure-sensitivity rubber modified epoxy adhesives is represented by the nucleation, growth and coalescence of voids and the formation of discrete shear bands for cavitated rubber particles (Cheng and Guo 2007).

Because of the complex geometry, material nonlinearity and large deformation of adhesive composite joints, finite element analysis (FEA) has become a powerful tool to study the delamination mechanisms of composites. Combined with the FEA, there are two main numerical methods which have been widely applied to the delamination research of composites: the virtual crack closure technique (VCCT) and the cohesive theory. The VCCT proposed by Rybicki and Kanninen (1977) can calculate the ERR more efficiently than J-integral (Krueger 2004; Liu and Yang 2014) because the requirement for mesh sizes is not high for the VCCT. Besides, the VCCT can predict the delamination crack growth well using FEA (Xie and Biggers 2006; Liu et al. 2011; Liu and Zheng 2013) based on the B–K law (Benzeggagh and Kenane 1996) or Power law. However, the VCCT within the framework of linear elastic fracture mechanics is not competent for predicting ductile failure of the adhesive layer with a finite-size nonlinear fracture process zone. By comparison, the cohesive theory proposed by Dugdale (1960) and Barenblatt (1962) has been demonstrated to be the most popular approach for predicting the delamination initi-

ation and growth of adhesive composite joint within the framework of elastic–plastic fracture mechanics (Yang et al. 1999; Gustafson and Waas 2009). The cohesive model assumes the interface failure is governed by a mathematical traction–displacement jump relationship which is related to the interface fracture toughness.

Currently, there are many cohesive models according to the shape of traction–displacement jump curves. Popular models include the polynomial cohesive model (Tvergaard 1990), the trapezoidal models (Tvergaard and Hutchinson 1993), the bilinear cohesive models (Geubelle and Baylor 1998; Alfano and Crisfield 2001; Camanho et al. 2003; Turon et al. 2006; Jiang et al. 2007), the linearly decreasing cohesive model (Camacho and Ortiz 1996), the discrete cohesive model (Xie and Waas 2006), the unified potential-based cohesive model (Park et al. 2009) and the exponential cohesive models (Xu and Needleman 1993; Ortiz and Pandolfi 1999; Goyal et al. 2004; Liu and Islam 2013; Liu et al. 2015). In particular, the extended finite element method with the embedded cohesive model is used to model the crack propagation along arbitrary path (Moës and Belytschko 2002; Xu and Yuan 2011; Liu 2015). Although these models are successfully applied to the delamination research of composites, most of them neglected the frictional contact effect during delamination. From the theoretical perspective, there is a continuous transition from the cohesive state to the frictional contact state related to the asperity deformation. Thus, a plausible two-step method including the first decohesion and then the friction was generally adopted. Tvergaard (1990) first considered both the cohesive failure and frictional contact effect by assuming the friction is activated after complete cohesive failure. Later, Chaboche et al. (1997) modified the polynomial cohesive model proposed by Tvergaard (1990), Lin et al. (2001) modified the bilinear cohesive model proposed by Geubelle and Baylor (1998) and Snozzi and Molinari (2013) modified the linearly decreasing cohesive model proposed by Camacho and Ortiz (1996) in order to describe continuous transition from the cohesive state to the frictional state.

However, the degradation process of cohesive zones is often accompanied by gradually increased friction from the physical perspective because the thickness of adhesive layers is very thin. In fact, the microscopic damage process of rubber modified epoxy matrix is also accompanied by the internal friction.

Wisnom and Jones (1996) highlighted the frictional effect in the mode-II shear delamination of composites by experiments. Later, Fan et al. (2007) proposed a unified approach to quantify the frictional effect using the mode-II delamination tests including the end-notched flexure (ENF), end-loaded-split (ELS), four-point bending ENF (4ENF) and over-notched-flexure (ONF). Their conclusions showed the friction plays an important role in affecting the delamination resistance. Therefore, a favorable strategy is to couple the cohesive model and friction in the delamination analysis. Raous et al. (1999) first proposed a micromechanical adhesion/friction coupled model by considering the contact zone as a material boundary. When the interface is decomposed into a damaged part with the friction and an undamaged part, Alfano and Sacco (2006) proposed a bilinear cohesive/friction coupled model. Later, Parrinello et al. (2009, 2013), Guiamatsia and Nguyen (2014) and Serpieri et al. (2015) extended the work of Alfano and Sacco (2006) by further considering the plastic interface and mixed-mode interface failure under different load conditions.

However, Liu and Islam (2013) showed the bilinear cohesive model cannot represent accurately the true nonlinear fracture process zone with such as the fiber bridging toughening mechanism and crack-tip plastic deformation in fiber-reinforced composites. Campilho et al. (2013) also pointed out the bilinear cohesive model is efficient for brittle adhesive failure under tension, but underestimates the failure strength of ductile adhesives with large plastic flow in shear. Besides, numerical convergence using FEA due to a sharp transition at the peak traction for the bilinear cohesive model is also a big trouble (Liu and Islam 2013; Campilho et al. 2013). By comparison, Campilho et al. (2013) showed the exponential and trapezoidal cohesive models are more suitable for ductile adhesive failure. Further, the exponential function with a continuous transition at the peak point is more suitable for modeling the delamination with the friction than the trapezoidal function from the mathematical perspective. Thus, a favorable strategy is to couple the exponential cohesive model with the friction to simulate the shear delamination of composites.

This paper originally proposes a nonlinear cohesive/friction coupled model for the mode-II shear delamination of adhesive composite joint based on a modified Xu and Needleman's exponential cohesive model, which includes a non-associative frictional slip criterion and a slip potential as well as a return mapping algorithm for the plastic frictional contact problem. The proposed model is implemented using zero-thickness interface element by ABAQUS-UEL, which is limited to small frictional sliding state. Then, the main purpose of numerical calculations is to predict the effects of the friction coefficient and cohesive strength on the load–displacement curves and delamination mechanisms of composites. Numerical results for the mode-II shear delamination of the $[0°]_6$, $[\pm 30°]_5$, $[\pm 45°]_5$ angle-ply end-notched flexure adhesive composite joints using FEA demonstrate the proposed model by comparing the analytical solutions.

2 Nonlinear cohesive/friction coupled model for mode-II delamination of composites

Mode-II shear delamination for an end-notched flexure (ENF) composite specimen with the frictional contact is shown in Fig. 1. The normal and tangential displacement jumps (or called separation) $[[u]]_n$ and $[[u]]_t$ are written as
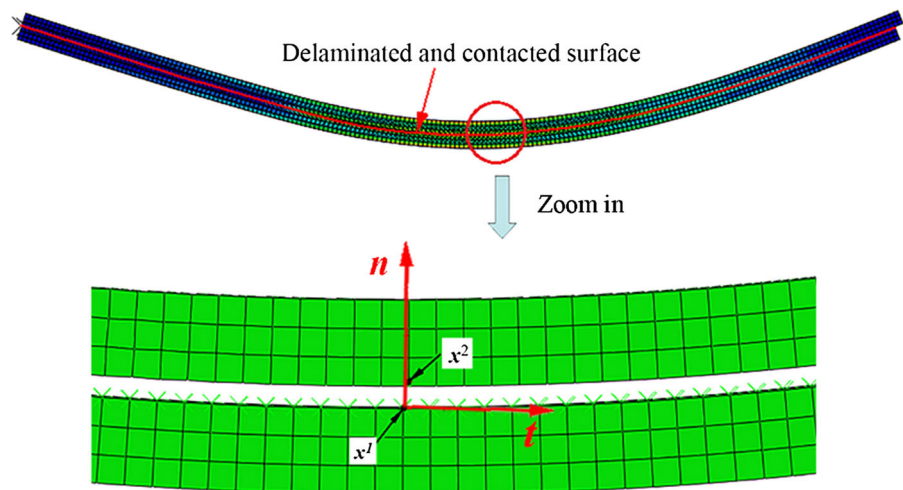
$$[[u]]_n = \left(x^1 - x^2 \right) \cdot n, \quad [[u]]_t = \left(x^1 - x^2 \right) \cdot t \quad (1)$$

where x^1 and x^2 are material points at the discontinuous interface, and n and t denote the normal and tangential directions. For the contacted interface, the non-penetration condition requires the inequality constraint $[[u]]_n \geq 0$ holds.

Xu and Needleman (1993) proposed an interface potential-based cohesive model which has been widely used for predicting the interface failure

$$\phi \left([[u]]_n, [[u]]_t \right)$$
$$= \phi_n + \phi_n \exp \left(-\frac{[[u]]_n}{\delta_n} \right) \left\{ \left(1 - r + \frac{[[u]]_n}{\delta_n} \right) \left(\frac{1 - q}{r - 1} \right) \right.$$
$$\left. - \left[q + \left(\frac{r - q}{r - 1} \right) \frac{[[u]]_n}{\delta_n} \right] \exp \left(-\frac{[[u]]_t^2}{\delta_t^2} \right) \right\},$$
$$T_n \left([[u]]_n, [[u]]_t \right)$$
$$= \frac{\partial \phi}{\partial [[u]]_n} = \frac{\phi_n}{\delta_n} \exp \left(-\frac{[[u]]_n}{\delta_n} \right) \left\{ \frac{[[u]]_n}{\delta_n} \exp \left(-\frac{[[u]]_t^2}{\delta_t^2} \right) \right.$$
$$\left. + \left(\frac{1 - q}{r - 1} \right) \left[1 - \exp \left(-\frac{[[u]]_t^2}{\delta_t^2} \right) \right] \left(r - \frac{[[u]]_n}{\delta_n} \right) \right\},$$

Fig. 1 Mode-II shear delamination for the ENF composite specimen with the frictional contact (x^1 and x^2 are separated material points at the discontinuous interface)

$$T_t \left([[u]]_n, [[u]]_t \right)$$
$$= \frac{\partial \phi}{\partial [[u]]_t}$$
$$= 2 \frac{\phi_n}{\delta_t} \frac{[[u]]_t}{\delta_t} \left[q + \left(\frac{r-q}{r-1} \right) \frac{[[u]]_n}{\delta_n} \right]$$
$$\times \exp \left(-\frac{[[u]]_n}{\delta_n} \right) \exp \left(-\frac{[[u]]_t^2}{\delta_t^2} \right),$$
$$\delta_n = \phi_n / \left[\sigma_{\max} \exp(1) \right], \delta_t = \phi_t / \left[\tau_{\max} (0.5 \exp(1))^{0.5} \right]$$
(2)

where ϕ is the interface potential including the normal and tangential parts ϕ_n and ϕ_t. T_n and T_t are the normal and tangential cohesive tractions. $\sigma_{\max}$ is the maximum normal traction without the tangential displacement jump and $\tau_{\max}$ is the maximum tangential traction without the normal displacement jump. The normal traction T_n reaches the maximum value $\sigma_{\max}$ at the normal displacement jump δ_n, and the tangential traction T_t reaches the maximum value $\tau_{\max}$ at the tangential displacement jump $\delta_t / \sqrt{2}$. Specially, Gao and Bower (2004) considered the interface potential as the fracture toughness. In the following, $G_I^c = \phi_n$ and $G_{II}^c = \phi_t$ are taken as the delamination fracture toughness in the normal and tangential directions, respectively. $q = \phi_t / \phi_n$ and $r = [[u]]_n^* / \delta_n$ are coupling constants between the normal and tangential directions. $[[u]]_n^*$ is the value of $[[u]]_n$ after complete shear separation with $T_n = 0$.

Abdul-Baqi and Van der Giessen (2002) and Hattiangadi and Siegmund (2005) suggested $q \approx 0.43$ so that the maximum tractions have the same values

$T_n = T_t$ at $\delta_n = \delta_t$. However, $\phi_n = \phi_t$ holds at $q = 1$, which is yet inconsistent with the experimental delamination results. In order to allow different values for ϕ_n and ϕ_t, van den Bosch et al. (2006) proposed a modified version of Xu and Needleman's cohesive model by taking $q = 1$ in Eq. (2) and replacing ϕ_n by ϕ_t in the expression of the traction T_t

$$\phi \left([[u]]_n, [[u]]_t \right)$$
$$= \phi_n \left[1 - \left(1 + \frac{[[u]]_n}{\delta_n} \right) \exp \left(-\frac{[[u]]_n}{\delta_n} \right) \exp \left(-\frac{[[u]]_t^2}{\delta_t^2} \right) \right],$$
$$T_n \left([[u]]_n, [[u]]_t \right)$$
$$= \frac{\phi_n}{\delta_n} \frac{[[u]]_n}{\delta_n} \exp \left(-\frac{[[u]]_n}{\delta_n} \right) \exp \left(-\frac{[[u]]_t^2}{\delta_t^2} \right),$$
$$T_t \left([[u]]_n, [[u]]_t \right)$$
$$= 2 \frac{\phi_t}{\delta_t} \frac{[[u]]_t}{\delta_t} \left(1 + \frac{[[u]]_n}{\delta_n} \right) \exp \left(-\frac{[[u]]_n}{\delta_n} \right) \exp \left(-\frac{[[u]]_t^2}{\delta_t^2} \right)$$
(3)

where the work done during mixed-mode separation is path-dependent at $\phi_n = \phi_t$.

Furthermore, McGarry et al. (2014) pointed out that unphysical behavior appears in the regions of mixed-mode overclosure using Eq. (3): the work of tangential separation reduces with increasing normal overclosure, and negative tangential work appears for large normal overclosure $[[u]]_n / \delta_n < -1$, resulting in repulsive tangential traction. In order to correct this problem, McGarry et al. (2014) modified Eq. (3) to the following non-potential form by removing the term $1 + [[u]]_n / \delta_n$

$$T_n \left([[u]]_n, [[u]]_t \right)$$
$$= \sigma_{\max} \exp(1) \frac{[[u]]_n}{\delta_n} \exp \left(-\frac{[[u]]_n}{\delta_n} \right) \exp \left(-\frac{[[u]]_t^2}{\delta_t^2} \right),$$

$T_t \left([[u]]_n, [[u]]_t\right)$

$$= \tau_{\max} \sqrt{2 \exp(1)} \frac{[[u]]_t}{\delta_t} \exp\left(-\frac{[[u]]_n}{\delta_n}\right) \exp\left(-\frac{[[u]]_t^2}{\delta_t^2}\right),$$

$$\delta_n = \phi_n / \left[\sigma_{\max} \exp(1)\right], \delta_t = \phi_t / \left[\tau_{\max} (0.5 \exp(1))^{0.5}\right] \quad (4)$$

In the following, a cohesive/friction coupled model based on Eq. (4) for the mode-II shear delamination of composites is proposed. After the tangential cohesive softening appears, non-associative plasticity interface with the frictional contact is assumed, where both the normal and tangential displacement jumps $[[u]]_n$ and $[[u]]_t$ are divided into the elastic and plastic parts $[[u]]_n = [[u]]_{n(e)} + [[u]]_{n(p)}$ and $[[u]]_t = [[u]]_{t(e)} + [[u]]_{t(p)}$. If the tangential traction-elastic displacement jump curve obeys the exponential distribution, Eq. (4) is further adjusted to the following form for the mode-II shear delamination with the normal contact

$$T_n \left([[u]]_{n(e)}\right) = K_n [[u]]_{n(e)},$$

$$\delta_t = \phi_t / \left[\tau_{\max} (0.5 \exp(1))^{0.5}\right],$$

$$T_t \left([[u]]_{t(e)}\right) = \tau_{\max} \sqrt{2 \exp(1)} \frac{[[u]]_{t(e)}}{\delta_t}$$

$$\exp\left(-\frac{[[u]]_{t(e)}^2}{\delta_t^2}\right),$$

$$K_t = \frac{\partial T_t}{\partial [[u]]_{t(e)}}$$

$$= \frac{\tau_{\max}}{\delta_t} \sqrt{2 \exp(1)} \exp\left(-\frac{[[u]]_{t(e)}^2}{\delta_t^2}\right)$$

$$\left(1 - \frac{2[[u]]_{t(e)}^2}{\delta_t^2}\right) \quad (5)$$

where the normal traction T_n is adjusted by introducing the normal penalty stiffness K_n based on the Kuhn–Tucker contact relationships $[[u]]_{n(e)} \geq 0$, $T_n \leq 0, [[u]]_{n(e)} T_n = 0$. K_t is the tangential stiffness which becomes negative at $[[u]]_{t(e)} \geq [[u]]_{t(e)}^0 = \sqrt{2}/2\delta_t$.

Remarks Currently, many numerical methods are proposed to deal with the contact constraint including the penalty method and the Lagrange multiplier method. Weyler et al. (2012) made a comprehensive review on these two methods. Although they lead to consistent formulations, there is some difference for numerical robustness. The Lagrange multiplier method introduces an additional variable (Lagrange multiplier) to enforce

the contact constraint. However, it introduces zero in the diagonal of the matrix, leading to some numerical difficulties. By comparison, the penalty method solves the interpenetration problem by introducing a large positive penalty parameter to satisfy the constraint condition. Theoretically, infinite penalty parameter leads to accurate enforcement of the constraint. In this research, the penalty method is used, but the penalty stiffness K_n must be appropriately chosen so that ill-conditioned problems can be avoided.

After the initial tangential cohesive softening appears, $\mu |T_n|$ (μ is the variable friction coefficient) is superimposed onto the tangential traction T_t to describe continuous transition from the cohesive state to the friction state explicitly. Thus, the tangential traction becomes $T_t + \mu |T_n|$. $\mu |T_n|$ increases exponentially from zero to the smooth value $\mu_s |T_n|$ ($\mu_s = \tan \phi$ is the smooth friction coefficient and ϕ is the friction angle) where pure frictional contact appears, as shown in Fig. 2. The variable friction coefficient μ is written as

$$\mu = \mu_s \frac{\exp(d) - 1}{\exp(1) - 1},$$

$$d = \frac{[[u]]_{t(e)}^c \left[[[u]]_{t(e)} - [[u]]_{t(e)}^0\right]}{[[u]]_{t(e)} \left[[[u]]_{t(e)}^c - [[u]]_{t(e)}^0\right]} \quad (6)$$
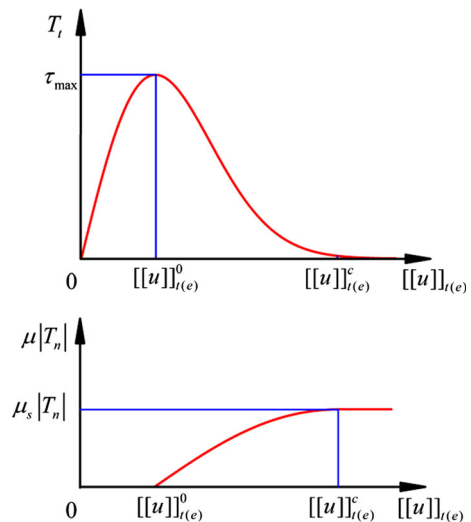
Fig. 2 Superimposed tangential friction increases exponentially from zero at the beginning of tangential cohesive softening to the smooth friction (friction coefficient is μ_s) at the complete tangential cohesive failure where pure frictional contact appears

where d is the damage-like variable which represents the intensity of adhesion. It is worth pointing out Raous et al. (1999) modeled the coupling between the adhesion, friction and unilateral contact, in which the adhesion is characterized as an internal variable similar to the damage variable d. $[[u]]_{t(e)}^0$ and $[[u]]_{t(e)}^c$ are the initial and critical displacement jumps, respectively. Based on Eq. (5), $[[u]]_{t(e)}^c$ is solved by assuming the area under the tangential traction–elastic displacement jump curve reaches the maximum

$$\frac{\int_0^{[[u]]_{t(e)}^c} \frac{[[u]]_{t(e)}}{\delta_t} \exp\left(-\frac{([[u]]_{t(e)})^2}{\delta_t^2}\right) \mathrm{d}[[u]]_{t(e)}}{\int_0^\infty \frac{[[u]]_{t(e)}}{\delta_t} \exp\left(-\frac{([[u]]_{t(e)})^2}{\delta_t^2}\right) \mathrm{d}[[u]]_{t(e)}}$$

$$= e \to 1 \Rightarrow [[u]]_{t(e)}^c = \delta_t \sqrt{-\ln(1-e)} \tag{7}$$

where $[[u]]_{t(e)}^c \approx 3\delta_t$ holds at $e = 0.9999$.

Remarks it is noted the exponential cohesive traction never reaches zero even at infinite crack opening separation. However, the actual critical separation $[[u]]_{t(e)}$ cannot reach infinity at the complete tangential failure. Therefore, a finite critical separation $[[u]]_{t(e)}^c$ is assumed in this research, which is solved by assuming the accumulative cohesive fracture energy reaches the maximum, similar to the work by Goyal et al. (2004) and Liu and Islam (2013).

The plastic deformation of adhesive materials in shear is non-associative. After the initial cohesive softening appears, the frictional contact problem resorts to the classic non-associative plasticity theory. Based on the work of Raous et al. (1999), Parrinello et al. (2009) and Weyler et al. (2012), the frictional slip criterion F and the slip potential G according to the non-associative Mohr–Coulomb frictional contact law are written as

$$F = T_t + \mu|T_n| - \mu_s|T_n|,$$
$$G = T_t + \beta_s|T_n|,$$
$$[[\dot{u}]]_{t(p)} = \dot{\lambda}\frac{\partial G}{\partial T_t} = \dot{\lambda}, \quad [[\dot{u}]]_{n(p)} = \dot{\lambda}\frac{\partial G}{\partial|T_n|}$$
$$= \beta_s\dot{\lambda} = \beta_s[[\dot{u}]]_{t(p)} \tag{8}$$

where $\dot{\lambda}$ is the consistency factor. F obeys the slip/stick (Kuhn–Tucker) conditions $F \leq 0$, $\dot{\lambda} \geq 0$ and $\dot{\lambda}F = 0$. $\beta_s = \tan(\varphi)$ is the dilatancy and φ ($0 \leq \varphi \leq \phi$) is the dilatant angle. In the Mohr–Coulomb plasticity model, the friction angle ϕ defines the ratio of the shear stress to the normal stress, and the
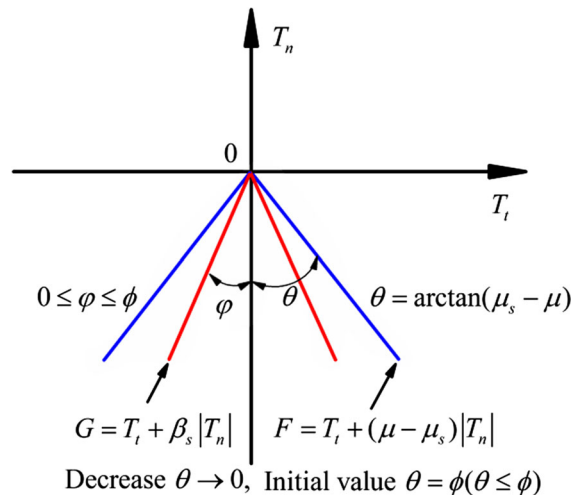
Fig. 3 Limit friction surfaces of the Coulomb law as a cone in the space of contact traction

dilatant angle φ denotes the ratio of the volumetric strain rate to the shear strain rate, and dilatancy β_s is the volume expansion in shear for adhesive materials. The limit friction surface $F = 0$ of the Coulomb law is a cone in the space of contact traction, as shown in Fig. 3. From Eq. (8), the normal and tangential plastic displacement jumps $[[u]]_{n(p)}$ and $[[u]]_{t(p)}$ take on the same increasing tendency.

Remarks Parrinello et al. (2009) proposed a bilinear cohesive/friction coupled interface model, where a non-associative frictional interface is considered. In this research, the tangential traction $T_t + \mu|T_n|$ by replacing T_t in their model is used in the slip criterion in Eq. (8).

After introducing the return mapping algorithm in "Appendix 1", the updated normal traction $\overline{T}_n = T_n([[u]]_{n(e)})$, the updated tangential traction $\overline{T}_t = \mu_s|T_n|([[u]]_{n(e)})$ and the tangential stiffness $K_t = K_t([[u]]_{t(e)})$ are obtained.

3 Finite element analysis and numerical results of composites with mode-II delamination

3.1 Numerical issues for the cohesive/friction coupled model

The boundary value problem with a discontinuous interface with the friction is shown in Fig. 4. Let us

Fig. 4 Boundary value problem with a discontinuous interface with the frictional contact. **a** Discontinuous interface with friction, **b** cohesive element for contact. Contact surfaces: m and s with small frictional sliding
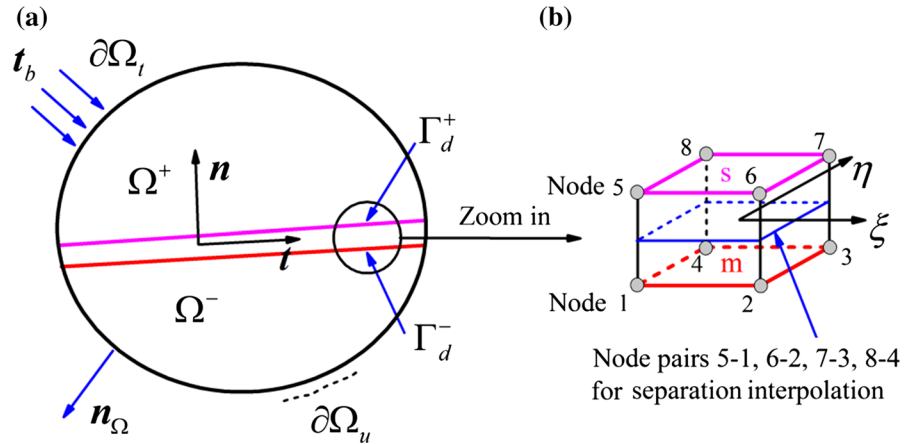
consider a bounded domain $\Omega \subset \mathbb{R}^{n_{\dim}}$ ($n_{\dim}$ denotes the space dimension) as an open and bounded set with an outward normal vector $\boldsymbol{n}_\Omega$. The smooth boundary $\partial\Omega$ is divided into either Neumann or Dirichlet boundary conditions defined on $\partial\Omega_t$ and $\partial\Omega_u$ respectively, such that $\partial\Omega = \partial\Omega_u \cup \partial\Omega_t$, $\partial\Omega_u \cap \partial\Omega_t = \varnothing$ and closure $\overline{\Omega} = \Omega \cup \partial\Omega$. Ω is divided into Ω^+ and Ω^- by an internal discontinuous interface Γ_d such that $\Omega = \Omega^+ \cup \Omega^-$. The displacement field $\boldsymbol{u}$ across Γ_d is discontinuous but continuous in Ω^+ and Ω^-. The normal vector $\boldsymbol{n}$ at the discontinuous interface points from Ω^- to Ω^+.

The weak form of boundary value problem is written as

$$
\int_{\Omega^+\cup\Omega^-} \nabla_X \delta\boldsymbol{u} : \boldsymbol{\sigma}\,\mathrm{d}V + \int_{\Gamma_d} \delta[[\boldsymbol{u}]] \cdot \boldsymbol{T}
$$
$$
\mathrm{d}A = \int_{\partial\Omega_t} \delta\boldsymbol{u} \cdot \boldsymbol{t}_b\,\mathrm{d}A \tag{9}
$$

where $\boldsymbol{u}_b : \partial\Omega_u \to \mathbb{R}^3$ is the field of prescribed displacement on the Dirichlet boundary and $\boldsymbol{t}_b : \partial\Omega_t \to \mathbb{R}^3$ is the field of prescribed traction on the Neumann boundary. $\boldsymbol{\sigma}$ is the Cauchy stress tensor. The Cauchy cohesive traction $\boldsymbol{T}$ which acts on the internal boundary Γ_d depends on the displacement jump $[[\boldsymbol{u}]]$ at the interface Γ_d. $\boldsymbol{u}$ lies in the space of admissible trial function $\mathcal{U} := \{\boldsymbol{u} : \overline{\Omega} \to \mathbb{R}^{n_{\dim}}; \boldsymbol{u} = \boldsymbol{u}_b \text{ on } \partial\Omega_u\}$ and $\delta\boldsymbol{u}$ lies in the space of admissible weight function $\mathcal{V} := \{\delta\boldsymbol{u} : \Omega \to \mathbb{R}^{n_{\dim}}; \delta\boldsymbol{u} = \boldsymbol{0} \text{ on } \partial\Omega_u\}$.

Foulk et al. (2000) and Segurado and LLorca (2004) proposed finite element formulations for implementing the cohesive model using the isoparametric middle-plane interpolation, which are applicable to the elastic, elastoplastic, viscoelastic and viscoplastic materials

under geometrically small deformation or finite deformation. A typical 3D finite element formulation under quasi-static loads is given in "Appendix 2", where a main work is to calculate the cohesive stiffness tensor and the residual force vector based on the Newton–Raphson algorithm. Wriggers (2006) pointed out that the isoparametric element within the frictional contact area does not allow large relative displacement. Thus, the proposed cohesive/friction model is limited to small deformation. In addition, these cohesive/frictional contact elements are considered as intermediate regions connecting the contacted master/slave surfaces in each discrete contact domain of the deformed body (Weyler et al. 2012).

For the mode-II delamination growth, only two contact states appear: stick and slip. Therefore, the virtual cohesive/contact work is further expanded as three parts

$$
\int_{\Gamma_d} \delta[[\boldsymbol{u}]] \cdot \boldsymbol{T}\,\mathrm{d}A
$$
$$
= \underbrace{\int_{A_n^N} T_n \delta[[u]]_{n(e)}\,\mathrm{d}A}_{\text{Normal contact}} + \underbrace{\int_{A_n^T} (T_t + \mu\,|T_n|)\,\delta[[u_t]]\,\mathrm{d}A}_{\text{Stick}}
$$
$$
+ \underbrace{\int_{A_n^N/A_n^T} \overline{T}_t \delta[[u]]_{t(e)}\,\mathrm{d}A}_{\text{Slip}} \tag{10}
$$

where A_n^N and A_n^T are the discrete normal and tangential cohesive/contact domains. For pure contact discretization, non-matching mesh is allowed to appear. Yet, it is important to choose appropriate mesh discretization in case of non-matching mesh because the penalty method is equivalent to a mixed method where the Babuska–Brezzi stability condition must

be satisfied (Wriggers 2006). Fortunately, isoparametric matching zero-thickness cohesive/contact element adopted in this research can avoid this problem.

The cohesive model naturally introduces a length scale parameter due to cohesive softening behavior, which is defined as the distance from the crack tip to the position where the maximum cohesive traction is attained (Yang and Cox 2005; Turon et al. 2007; Harper and Hallett 2008). If the length scale is not considered in the delamination analysis, the dissipation of delamination fracture energy cannot be accurately captured which will lead to mesh sensitivity problem. Thus, the cohesive zone length must be properly evaluated. Further, there exist different length scales (or cohesive zone length) for different delamination fracture modes. Yang and Cox (2005), Turon et al. (2007) and Harper and Hallett (2008) evaluated the cohesive zone length by comparing existing theoretical formulas based on the crack-tip stress and energy fields. They showed the cohesive zone length is about 2–3 element side length. In this research, the cohesive zone length for the mode-II delamination is calculated in this way to regularize the delamination fracture toughness based on the smeared crack band model (Bažant and Oh 1983).

The proposed model is implemented by ABAQUS-UEL (user element subroutine) and the numerical algorithm using FEA is shown in Fig. 5. After the tangential cohesive softening appears, the tangential trial traction is calculated. If the frictional slip appears, Newton iterations are performed to calculate the updated normal and tangential tractions and stiffnesses. Then, the node residual force and element stiffness are calculated for solving the node displacement increment. It is noted that Newton–Cotes integration rather than Gaussian integration in ABAQUS-UEL is adopted to guarantee numerical robustness because Gaussian integration leads to oscillating load response at large stress gradient over the interface element (Schellekens and Borst 1993).

Convergence is also an important issue due to cohesive softening behavior. Here, a viscous force vector f_v is introduced into the residual equations to improve the convergence

$$\begin{cases} f_{ext} - f - f_v = R, \\ f_v = cM^*v, \ v = \Delta u/\Delta t \end{cases} \qquad (11)$$

where M^* is an artificial mass matrix calculated with unity density, v is the vector of node velocity, c is a constant damping factor and Δt is the time increment during nonlinear numerical iterations. f_{ext} is the external node force, f is the cohesive node force in Eq. (20) and R is the tolerance. It is noted that introduced viscous damping should be sufficiently large to regularize cohesive softening behavior but small enough not to affect numerical accuracy. Very small time increment is required to ensure numerical precision (the initial, minimum and maximum time increments are 0.0001, 1e−10 and 0.001 s, respectively).

3.2 Numerical results and discussion for the delamination of ENF adhesive joints

The end-notched flexure (ENF) glass/polyester composite specimens with an initial middle-plane delamination crack are shown in Fig. 6. Three types of layup specimens $[0°]_6$, $[\pm30°]_5$ and $[\pm45°]_5$ are used. These specimens were first studied by Ozdil et al. (1998) using analytical and numerical approaches and later studied by Theotokoglou and Vrettos (2006) using FEA. Geometry parameters are listed in Table 1 and material parameters are listed in Table 2 (Ozdil et al. 1998), in which the delamination fracture toughness is calculated using four methods: 1 Compliance theory (Broek 1984), 2 Beam theory (Russell and Street 1982), 3 Modified beam theory (Carlsson et al. 1986) and 4 Associated beam theory and first-order shear deformation theory (Ozdil et al. 1998). The formulas for four methods are attached in "Appendix 3". It is worth pointing out that the cohesive/friction model proposed by Parrinello et al. (2009, 2013) allows only the same delamination fracture toughness for the mode-I and II delamination. In fact, the mode-I fracture toughness is not necessary for the mode-II shear delamination. Although the friction affects the mode-II delamination fracture toughness (Carlsson et al. 1986), our purpose is to explore the effects of the cohesive strength and friction on the delamination mechanisms and load responses of composites at a constant mode-II delamination fracture toughness, similar to the work by Parrinello et al. (2009, 2013). Thus, the average value of the upper and lower limits of the delamination fracture toughness using four methods is used in this research. Three finite element models with different mesh sizes

**Fig. 5** Numerical algorithm for implementing the cohesive/friction coupled model using FEA
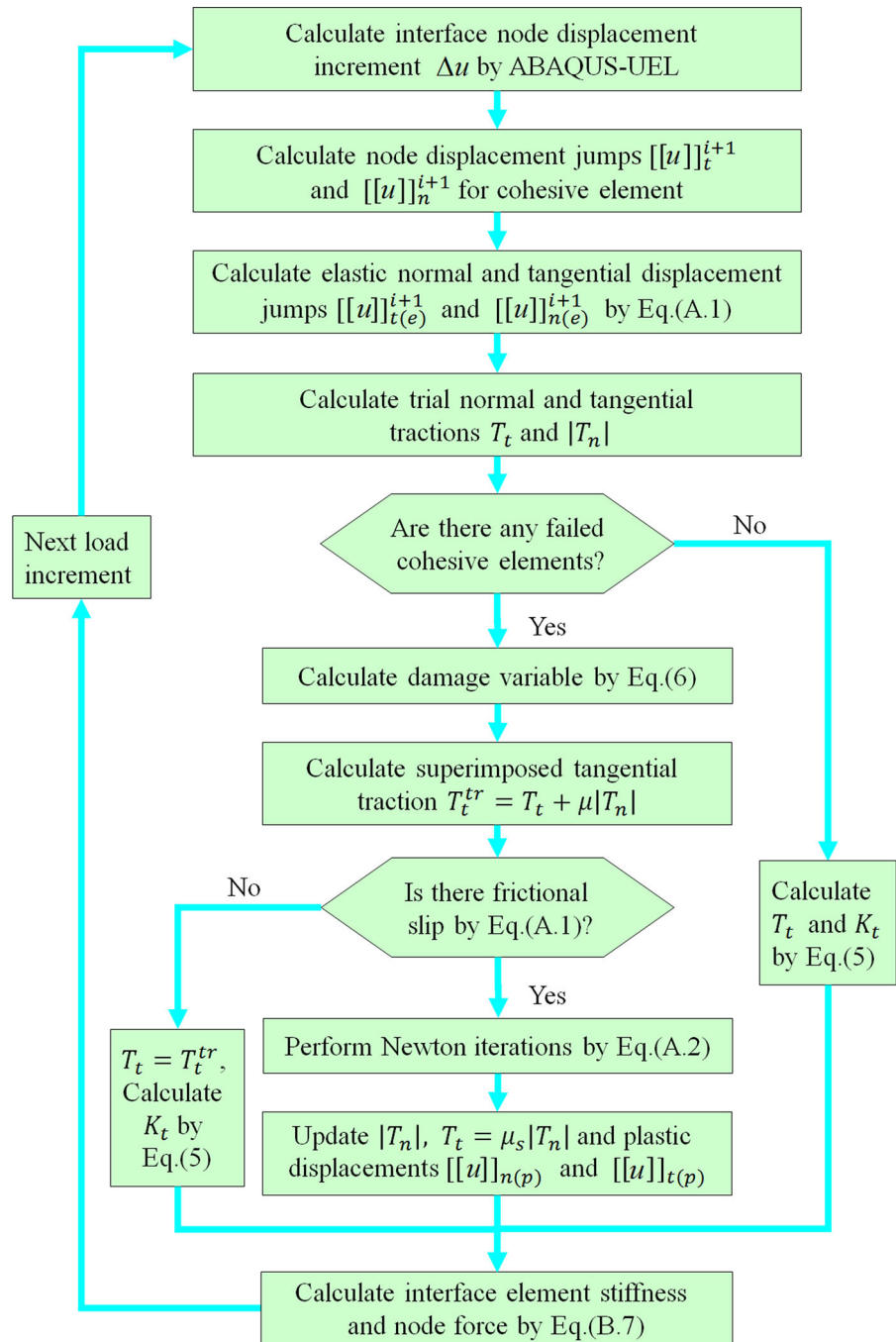
are shown in Fig. 7, where the number of bulk and cohesive elements for three mesh models and three layups is listed in Table 3.

First, the effect of viscous constant c in Eq. (11) on the load–displacement curves for Case-A lami-

nate using two mesh models is shown in Figs. 8 and 9. Numerical results by the proposed model are also compared with the analytical results without considering the frictional effect using the theoretical formulas derived by Mi et al. (1998), as attached in "Appen-

Fig. 6 Geometry of the ENF composite specimen
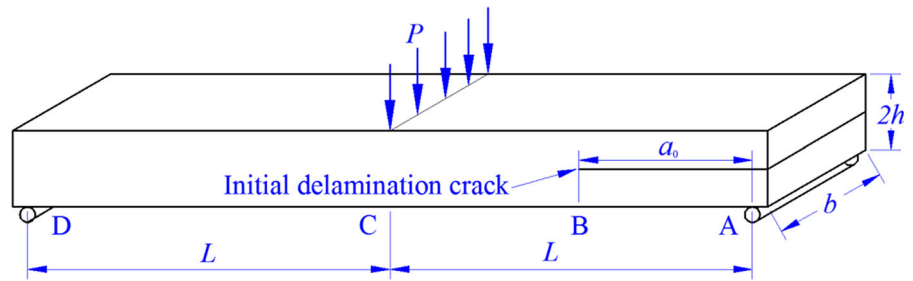
Table 1 Mechanical properties of quasi-unidirectional glass/polyester composites (Ozdil et al. 1998)

Ply longitudinal modulus	E_1	34.7 GPa
Ply transverse modulus	E_2	8.50 GPa
Out-of-plane modulus	E_3	8.50 GPa
Inplane shear modulus	G_{12}	4.34 GPa
Out-of-plane shear modulus	G_{13}	4.34 GPa
	G_{23}	3.27 GPa
Poisson's ratio	v_{12}	0.27
	v_{13}	0.27
	v_{23}	0.30
Mode-II delamination fracture toughness	G_{II}^{c}	0.496 ± 0.135 N/mm ($[0°]_6$)
		0.976 ± 0.071 N/mm ($[\pm30°]_5$)
		1.485 ± 0.158 N/mm ($[\pm45°]_5$)

Table 2 Geometry sizes of glass/polyester composite specimens (Ozdil et al. 1998)

Case	Layup	$2L$ (mm)	b (mm)	$2h$ (mm)	a_0 (mm)
A	$[0°]_6$	100	20	4.38	25
B	$[\pm30°]_5$	100	20	7.30	25
C	$[\pm45°]_5$	100	20	7.30	25

Fig. 7 Three finite element models for the ENF laminate with loads and boundary conditions. **a** Coarse mesh model, **b** middle mesh model, **c** fine mesh model
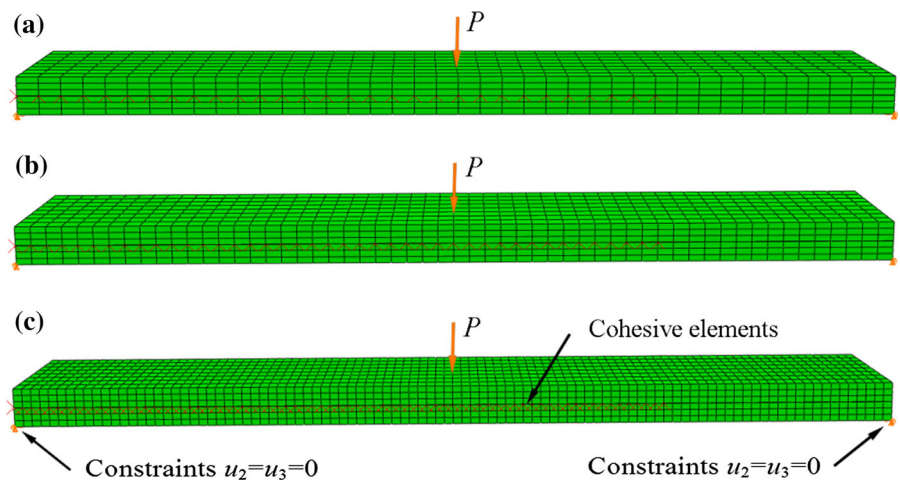
Table 3 Number of the bulk and cohesive elements for three mesh models and three layups

Layup	Number of bulk elements	Number of cohesive elements	Sizes of bulk elements: length × width × height (mm × mm × mm)
Coarse mesh			
Case-A	2688	336	1.78 × 2.5 × 0.73
Case-B and C	4480		
Middle mesh			
Case-A	4800	600	1.0 × 2.5 × 0.73
Case-B and C	8000		
Fine mesh			
Case-A	6720	840	0.71 × 2.5 × 0.73
Case-B and C	11,200		

dix 4". Second, coarse mesh size leads to numerical oscillation at the decreasing stage of load–displacement curves (Xie and Waas 2006; Liu and Islam 2013; Liu et al. 2015). The main reason arises from the sudden release of strain energy and the instantaneous failure of elements in the intralaminar materials, leading to non-physical limit points in the form of a snap-through or a snap-back situation in the load–displacement curves. However, oscillation does not represent large loss of accuracy for load responses. By comparing Fig. 8 with 9, fine mesh sizes along the direction of crack propagation helps to alleviate the oscillation largely by capturing the sudden release of strain energy during decreasing stage more precisely. It is believed finer mesh sizes can eliminate the oscillation completely. Besides, the viscous parameter c produces very small impact on the oscillation, compared with large sensitivity for mesh sizes. However, it is noted too large value for c will lead to inaccurate results indeed due to additionally dissipated viscous energy, but too small value for c will add the convergence difficulty. From Figs. 8 and 9, $c = 1e-4$ is a good choice in this research for achieving favorable combination of numerical convergence and accuracy, which is used in the following analysis. In summary, robust and accurate results can be obtained as long as mesh sizes and viscous constant are properly selected.

Third, the effect of normal stiffness K_n on the load–displacement curves using two mesh models for Case-A laminate is shown in Fig. 10. It is found when K_n is larger than 9000 N/mm^3 or smaller than 3000 N/mm^3, convergence becomes difficult at $c = 1e-4$. By com-
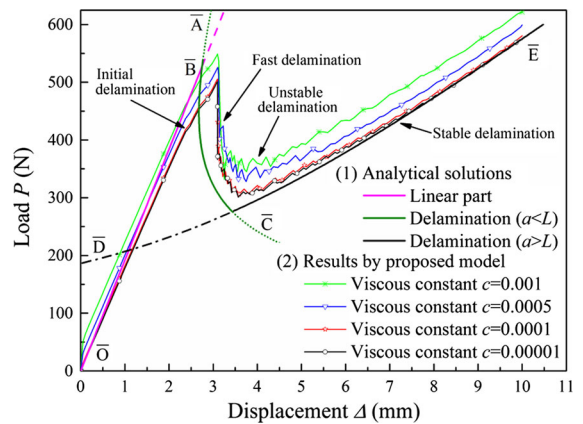

Fig. 8 Effect of the viscous constant c on the load–displacement curves for Case-A laminate at $\phi = 0°$ and $\tau_{max} = 30$ MPa using middle mesh model
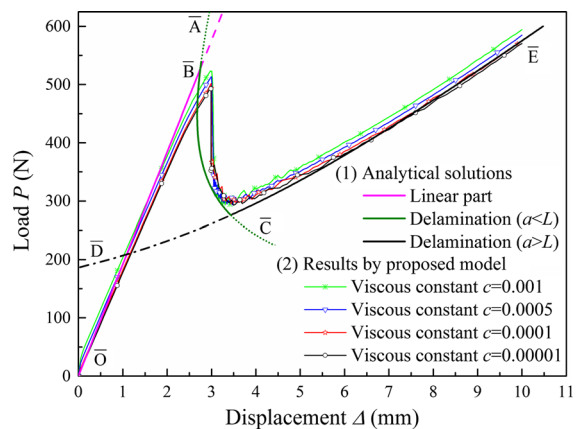
Fig. 9 Effect of the viscous constant c on the load–displacement curves for Case-A laminate at $\phi = 0°$ and $\tau_{max} = 30$ MPa using fine mesh model
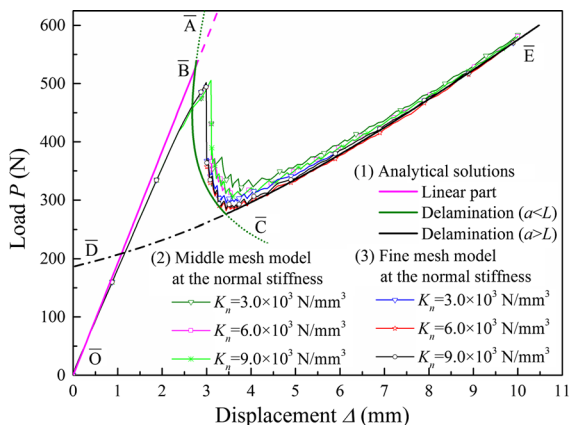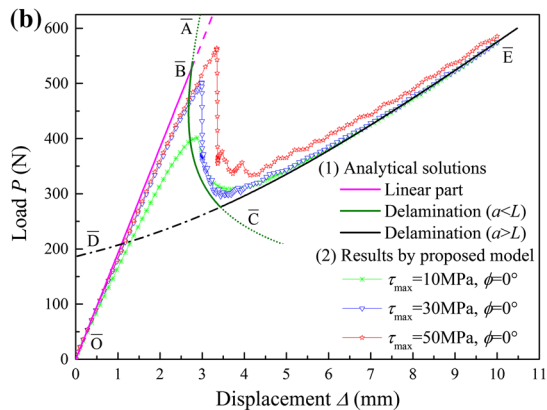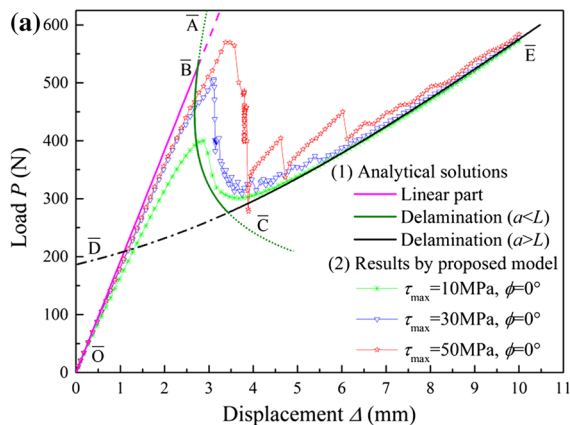
Fig. 10 Effect of the normal stiffness on the load–displacement curves for Case-A laminate at $\phi = 0°$ and $\tau_{max} = 30$ MPa using fine and middle mesh models
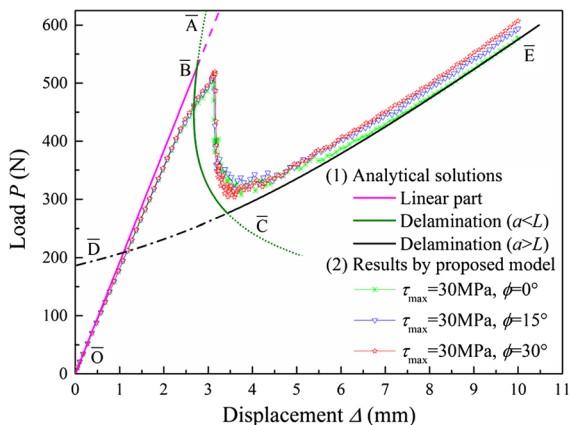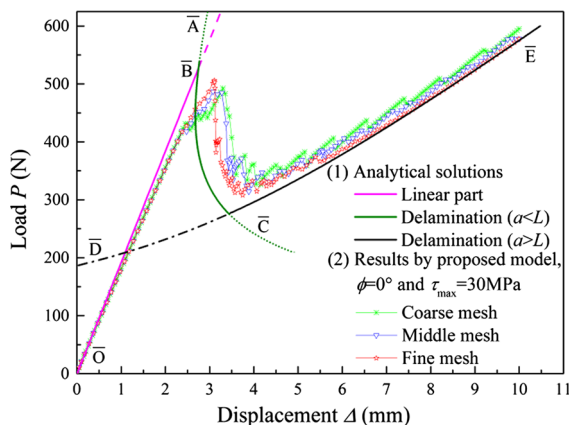

Fig. 11 Load–displacement curves for Case-A laminate using three friction angles and middle mesh model
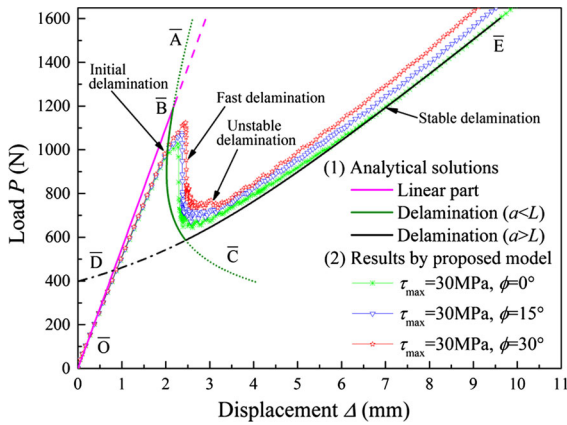

Fig. 12 Load–displacement curves for Case-A laminate using three cohesive strengths and **a** middle mesh model and **b** fine mesh model

Fig. 13 Load–displacement curves for Case-A laminate using three mesh models

parison, $K_n = 3000 - 9000$ N/mm^3 leads to good convergence at $c = 1e-4$. Thus, $K_n = 6000$ N/mm^3 is adopted in the following analysis.

The effects of the friction coefficient μ_s, cohesive strength τ_{max} and mesh size on the load–displacement curves for three cases are shown in Figs. 11, 12, 13, 14, 15, 16, 17, 18 and 19. Numerical results by the proposed model are also compared with the analytical results. For angle-ply laminates, equivalent moduli (Theotokoglou and Vrettos 2006) are used for analytical solutions. First, Schön (2000) measured the friction coefficient for the epoxy with frictional sliding against metal, where the friction is related to the shear deformation or fracture of the polymer surface. They obtained the friction coefficients 0.2–0.7 in the rubber region. In this research, we take three friction angles $\phi = 0°$, $15°$ and $30°$ and three fric-

Fig. 14 Load–displacement curves for Case-B laminate using three friction angles and middle mesh model

Fig. 15 Load–displacement curves for Case-B laminate using three cohesive strengths and **a** middle mesh model and **b** fine mesh model
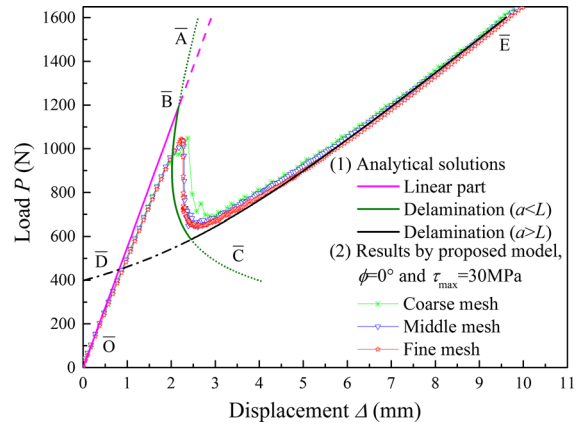

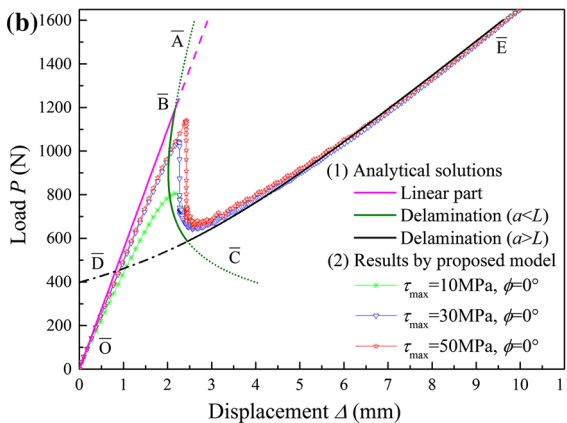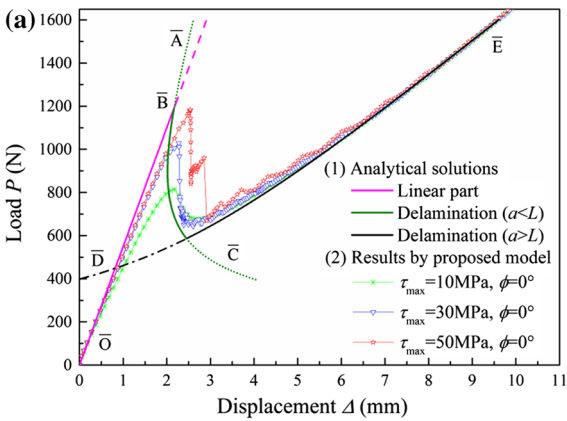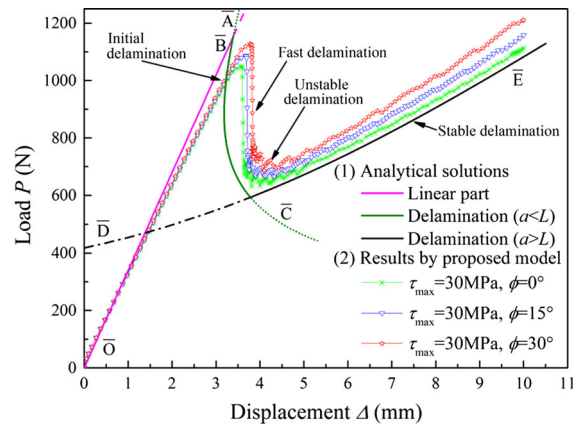**Fig. 16** Load–displacement curves for Case-B laminate using three mesh models

Fig. 17 Load–displacement curves for Case-C laminate using three friction angles and middle mesh model

tion coefficients are calculated as $\mu_s = \tan\phi = 0$, 0.27 and 0.54, respectively. From Figs. 11, 14 and 17, the frictional effect appears at the initial unstable

delamination stage $a = L$ and large friction coefficient leads to large peak load and slight oscillating load response. After the stable delamination stage is reached, the difference between the load curves using different friction coefficients becomes large, represented by large contact area and frictional energy dissipation. Besides, the frictional effects are larger for angle-ply Case-B and C laminates than unidirectional Case-A laminate. Second, take Case-A laminate for example, the delamination starts and the crack-tip energy dissipates as the displacement Δ increases to about 3.1 mm. As the crack propagates from $a = 25$ to 35 mm, the load response starts to change suddenly. From $\Delta = 3.1$ to 5.5 mm displacements, the unstable delamination is represented by oscillating load
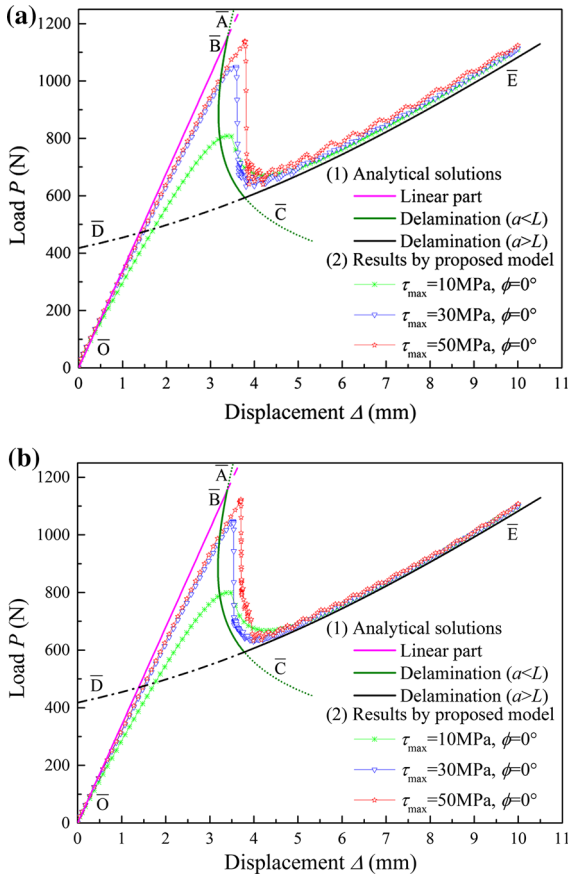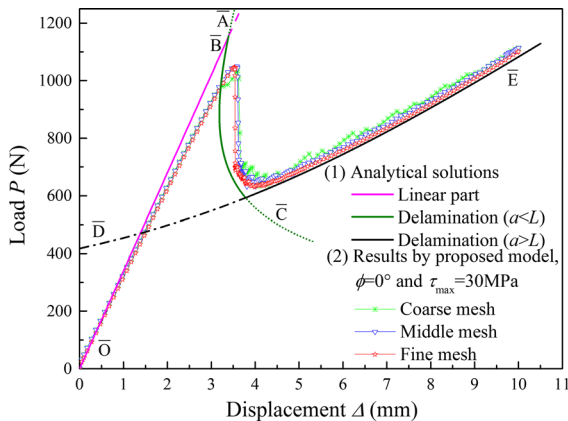
Fig. 18 Load–displacement curves for Case-C laminate using three cohesive strengths and **a** middle mesh model and **b** fine mesh model


**Fig. 19** Load–displacement curves for Case-C laminate using three mesh models

response. After $\Delta = 5.5$ mm displacement, the stable delamination stage appears and the frictional effect increases. Third, the stiffness of specimens increases slightly when τ_{max} adds. In addition, τ_{max} also affects the peak load for three cases, as shown in Figs. 12, 15 and 18. However, large value $\tau_{max} = 50$MPa will lead to convergence difficulty and oscillating load responses during the unstable delamination. Fourth, from Figs. 13, 16 and 19, the load curves using three mesh models (element side sizes along the crack propagation direction are 1, 1.8 and 2.5 mm respectively) are consistent. Although fine mesh model helps to eliminate the numerical oscillation, computational efficiency should also be considered, especially at large τ_{max}.

Delamination growth processes for Case-A laminate are shown in Fig. 20. The crack length-load displacement curves by discussing the effects of the friction coefficient and layup are shown in Figs. 21 and 22. The contours of shear stress τ_{13} for three cases at different stages are shown in Figs. 23, 24 and 25. The crack tip and the crack propagation length are determined by detecting the dislocated paired nodes for cohesive elements in Fig. 20 and the high-gradient area for the shear stress τ_{13} in Fig. 23. First, we approximately divide the whole delamination process into the fast delamination stage from $a = 25$ mm at $\Delta = 3.1$ mm to about $a = 45$ mm at $\Delta = 3.6$ mm, and the unstable delamination stage from $a = 45$ to 55 mm at $\Delta = 4.0$ mm, and the stable delamination stage at $a > 55$ mm for Case-A laminate. Second, the frictional effect is not distinct for the unidirectional Case-A laminate, which is represented by a small change of the shear stress τ_{13} when the friction coefficient increases. However, the frictional effect becomes distinct for angle-ply laminates as shown in Figs. 11, 14 and 17. Table 4 lists the bending strengths by comparing the effects of the layup, friction coefficient and cohesive strength. It is shown that large friction angle and cohesive strength lead to large strength, especially for angle-ply laminates. Third, the crack propagation rate is faster for Case-B laminate than that for Case-C laminate because the displacement Δ increases from 2.3 to 3.2 mm for Case-B laminate and from 3.7 to 4.9 mm for Case-

Fig. 20 Delamination growth processes for Case-A laminate at the displacement **a** 3.11 mm, **b** 4.34 mm and **c** 8.79 mm respectively at $\tau_{max} = 30$ MPa and $\phi = 45°$ using middle mesh model
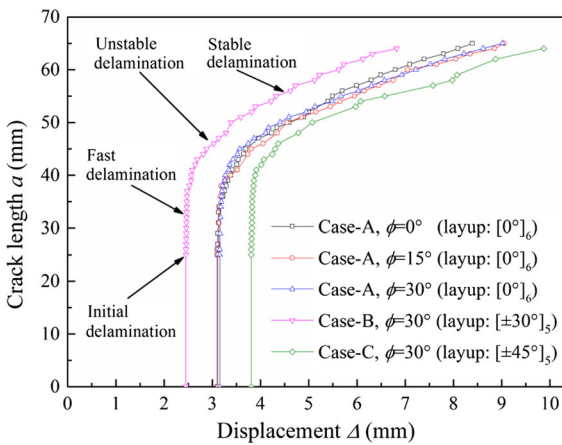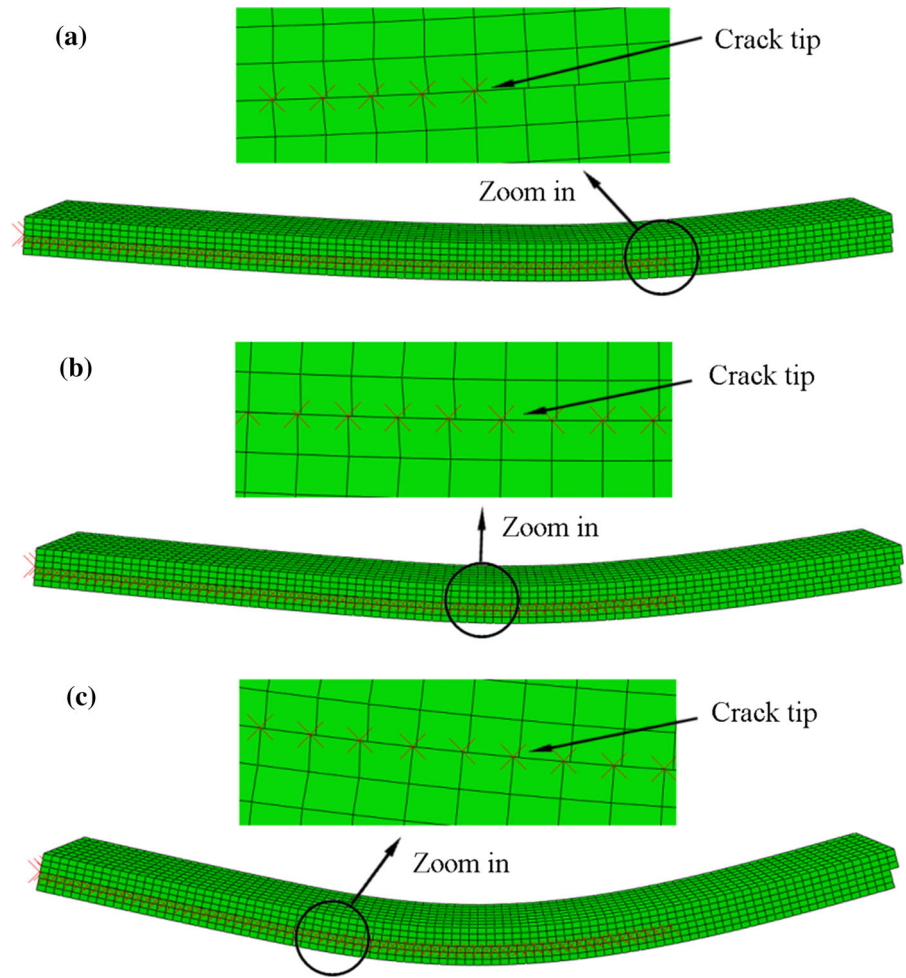
Fig. 21 Layup effect on the crack propagation rate at $\tau_{max} = 30$ MPa using middle mesh model
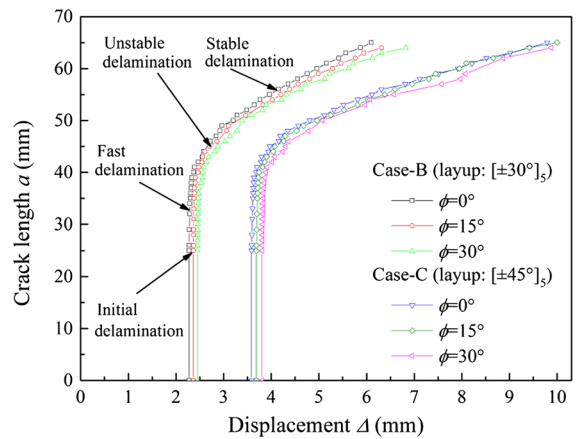
Fig. 22 Frictional effect on the crack propagation rate at $\tau_{max} = 30$ MPa using middle mesh model

Fig. 23 Contours of the tangential stress τ_{13} at the displacement **a** 3.12 mm, **b** 3.65 mm, **c** 4.85 mm and **d** 8.95 mm respectively for Case-A laminate at $\phi = 0°$ and $\tau_{max} = 30$ MPa using middle mesh model
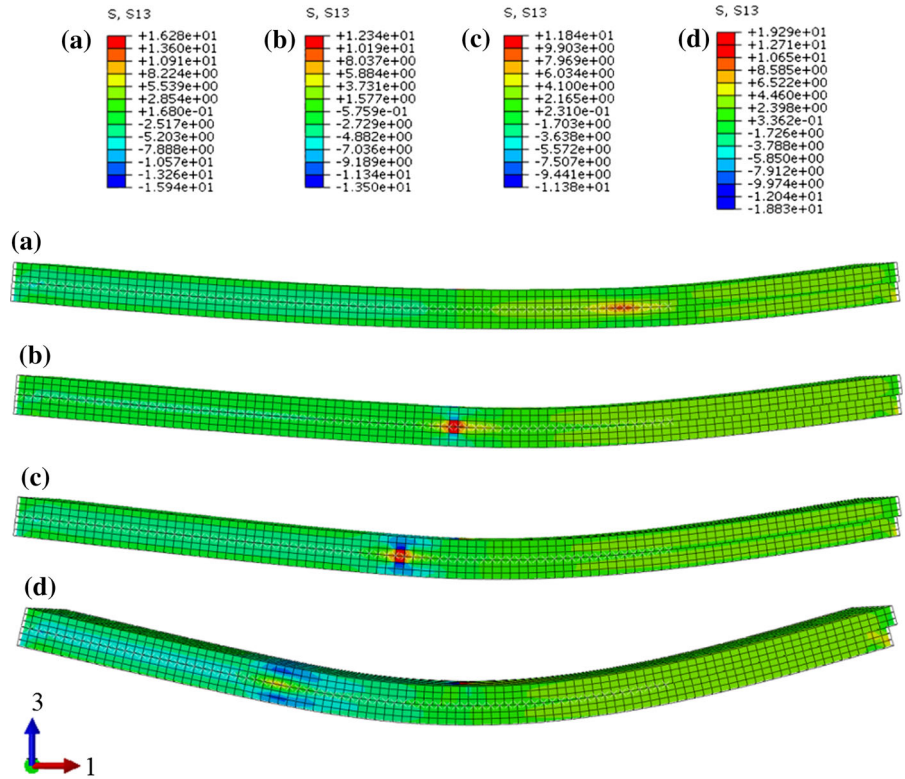
Fig. 24 Contours of the shear stress τ_{13} at the displacement **a** 3.12 mm, **b** 3.65 mm, **c** 4.85 mm and **d** 8.95 mm respectively for Case-A laminate at $\phi = 15°$ and $\tau_{max} = 30$ MPa using middle mesh model
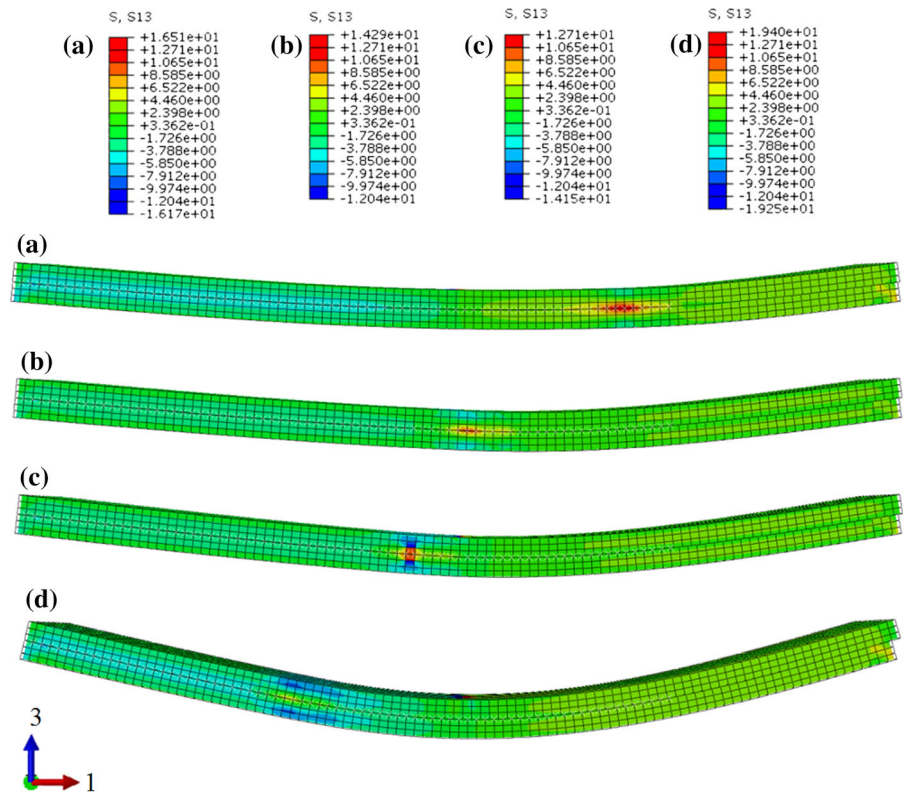
Fig. 25 Contours of the shear stress τ_{13} at the displacement **a** 3.12 mm, **b** 3.65 mm, **c** 4.85 mm and **d** 8.95 mm respectively for Case-A laminate at $\phi = 30°$ and $\tau_{max} = 30$ MPa using middle mesh model

C laminate as the crack propagates from $a = 25$ to 50 mm.

The effect of the superimposed traction $\mu |T_n|$ in Eq. (8) on the load–displacement curves are shown in Fig. 26. For unidirectional Case-A laminate, $\mu |T_n|$ has almost no effect o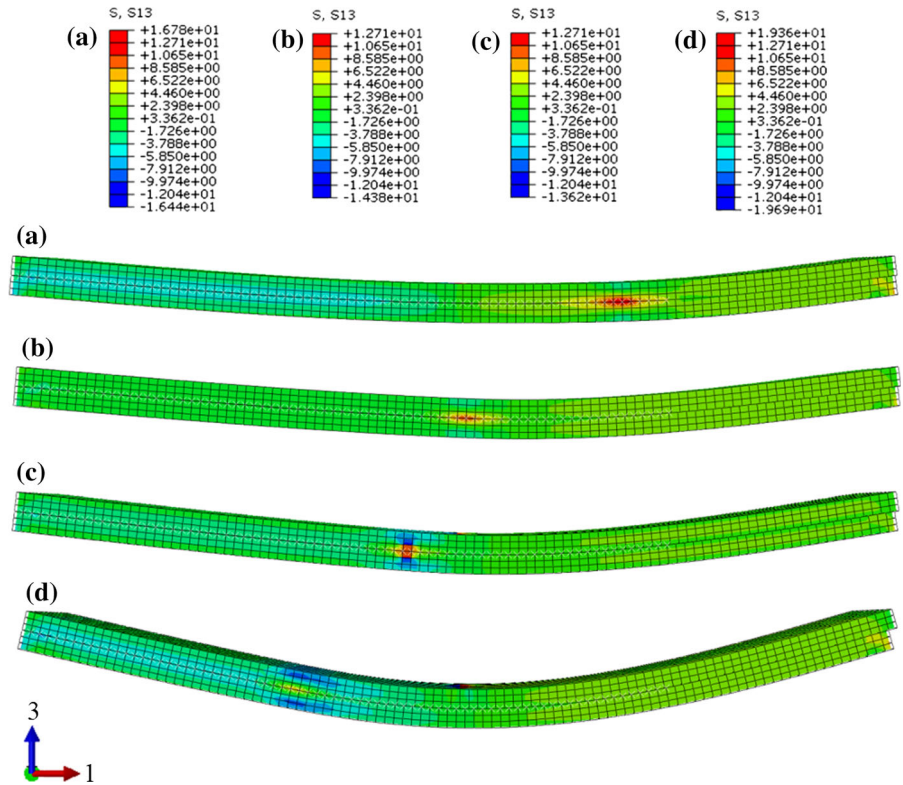n the load–displacement curves, but becomes a little more distinct for angle-ply Case-C laminate. By comparison, the introduction of $\mu |T_n|$ decreases the load-bearing ability slightly after the laminate enters into the unstable delamination stage for Case-C laminate.

4 Concluding remarks

This paper originally proposes a cohesive/friction coupled model for the mode-II shear delamination of angle-ply adhesive composite joint based on a modified Xu and Needleman's exponential cohesive model. The tangential friction is assumed to appear after the initial tangential cohesive failure, and the exponentially increased tangential friction is superimposed onto the tangential cohesive traction to describe continu-ous transition from the cohesive state to the frictional state explicitly. Then, a frictional slip criterion and a slip potential function as well as a numerical algorithm using FEA are proposed to solve the updated normal and tangential tractions and stiffnesses. Some important numerical issues for the proposed model are discussed in the FEA including the numerical interpolation technique for the cohesive element, the numerical convergence and the frictional contact algorithm based on the discrete contact domain. Numerical results on the $[0°]_6$, $[\pm 30°]_5$ and $\pm 45°]_5$ angle-ply end-notched flexure (ENF) composite specimens demonstrate the proposed model by comparing the analytical results. The main purpose of numerical calculations is to discuss the effects of the friction coefficient, tangential cohesive strength and normal contact stiffness on the load responses and delamination mechanisms of composites. It is shown the frictional effect becomes distinct after the unstable delamination for angle-ply laminates, leading to slightly stronger load-bearing ability. The proposed model and numerical technique will be applied to the frictional delamination for a series of aircraft structures.

Table 4 Bending strengths predicted using proposed model (Unit: N)

Layup	Middle mesh size, $\phi = 0°$, τ_{max}			$\tau_{max} = 30$ MPa, Middle mesh size		$\tau_{max} = 30$ MPa, $\phi = 0°$	
	10 MPa	30 MPa	50 MPa	$\phi = 15°$	$\phi = 30°$	Coarse mesh size	Fine mesh size
$[0°]_6$	399.9	505.9	569.9	511.5	519.4	484.9	481.6
$[\pm 30°]_5$	814.8	1028.4	1181.1	1077.1	1124.1	1048.9	1044.9
$[\pm 45°]_5$	808.3	1049.0	1136.8	1085.8	1127.9	1034.4	1046.4
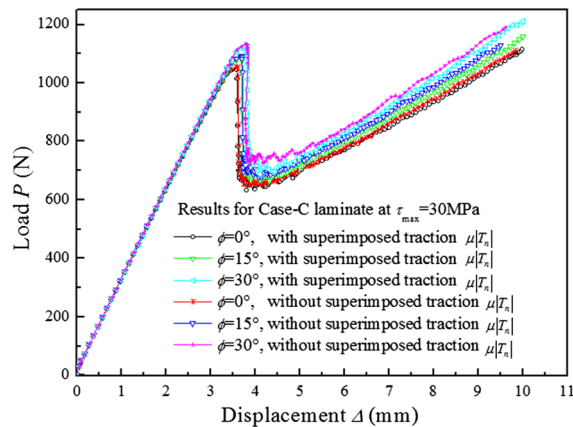
Fig. 26 Numerical results by considering the effect of the superimposed tangential traction $\mu |T_n|$ for Case-C laminate at $\tau_{max} = 30$MPa using middle mesh model

Appendix 1: Cohesive/friction contact algorithm using FEA

By referring to the return mapping algorithm, the updated tangential traction T_t and the consistent tangential stiffness K_t are solved by the following Newton iterations:

(a) After the tangential cohesive softening appears, the trial tangential traction is calculated as

$$T_t^{tr(i+1)} = T_t^{(i+1)} \left([[u]]_{t(e)}^{tr(i+1)} = [[u]]_t^{(i+1)} - [[u]]_{t(p)}^{(i)} \right)$$
$$+ \mu |T_n|^{(i+1)} \left([[u]]_{n(e)}^{tr(i+1)} = [[u]]_n^{(i+1)} - [[u]]_{n(p)}^{(i)} \right)$$
$$\tag{12}$$

where $[[u]]_t > 0$ and $[[u]]_n < 0$ are the normal and tangential displacement jumps at the beginning of new $(i+1)$th increment, and $[[u]]_{n(p)}^{(i)}$ and $[[u]]_{t(p)}^{(i)}$ are the normal and tangential plastic displacement jumps at the end of ith increment.

(b) If $T_t^{tr(i+1)} \leq \mu_s |T_n|^{(i+1)}$, the tangential stiffness $K_t \left([[u]]_t^{(i+1)} = [[u]]_{t(e)}^{tr(i+1)} \right)$ and the tangential traction $T_t = T_t^{tr(i+1)} = T_t \left([[u]]_t^{(i+1)} = [[u]]_{t(e)}^{tr(i+1)} \right)$ in Eq. (5) are calculated. There is no plastic loading and slip for the contacted interface.

(c) If $T_t^{tr(i+1)} > \mu_s |T_n|^{(i+1)}$, the plastic loading and frictional slip appear. After the initial value for $\Delta\lambda = 0$ is given, the following Newton iterations are performed to solve the updated elastic displacement jump $[[u]]_{t(e)}^{(i+1)}$ and the plastic displacement jump $[[u]]_{t(p)}^{(i+1)}$

$$T_t^{(i+1)} = \tau_{max} \sqrt{2 \exp(1)} \frac{\left| [[u]]_{t(e)}^{(i+1)} \right|}{\delta_t}$$
$$\exp\left[-\frac{\left([[u]]_{t(e)}^{(i+1)} \right)^2}{\delta_t^2} \right] > 0,$$

$$|T_n|^{(i+1)} = K_n \left| \left([[u]]_{n(e)}^{(i+1)} \right) \right| > 0,$$

$$F = T_t^{(i+1)} + \mu^{(i+1)} |T_n|^{(i+1)} - \mu_s |T_n|^{(i+1)},$$

$$G = T_t^{(i+1)} + \beta_s |T_n|^{(i+1)},$$

$$F + \frac{\partial F}{\partial \Delta\lambda} d\Delta\lambda + \cdots = 0$$
$$\Rightarrow d\Delta\lambda = -F/d_t > 0$$
$$\Rightarrow \Delta\lambda^{(i+1)} = \Delta\lambda^{(i)} - F^{(i+1)}/d_t^{(i+1)} > 0,$$

$$d_t^{(i+1)} = \left.\frac{\partial F}{\partial \Delta\lambda}\right|^{(i+1)}$$

$$= K_t^{(i+1)} + \beta_s \left(\mu^{(i+1)} - \mu_s\right) K_n < 0,$$

$$\mu^{(i+1)} = \mu_s \frac{\exp\left(d^{(i+1)}\right) - 1}{\exp\left(1\right) - 1},$$

$$K_t^{(i+1)} = \frac{\tau_{\max}}{\delta_t} \sqrt{2 \exp\left(1\right)}$$

$$\times \exp\left[-\frac{\left([[u]]_{t(e)}^{(i+1)}\right)^2}{\delta_t^2}\right]$$

$$\times \left(1 - \frac{2\left([[u]]_{t(e)}^{(i+1)}\right)^2}{\delta_t^2}\right) < 0,$$

$$[[u]]_{t(p)}^{(i+1)} = [[u]]_{t(p)}^{i} + \Delta\lambda^{(i+1)} > 0,$$

$$[[u]]_{t(e)}^{(i+1)} = [[u]]_{t}^{(i+1)} - [[u]]_{t(p)}^{(i+1)} > 0,$$

$$[[u]]_{n(p)}^{(i+1)} = [[u]]_{n(p)}^{(i)} + \beta_s \Delta\lambda^{(i+1)} > 0,$$

$$[[u]]_{n(e)}^{(i+1)} = [[u]]_{n}^{(i+1)} - [[u]]_{n(p)}^{(i+1)} < 0,$$

$$d^{(i+1)} = \frac{[[u]]_{t(e)}^{c}}{[[u]]_{t(e)}^{c} - [[u]]_{t(e)}^{0}} \left(1 - \frac{[[u]]_{t(e)}^{0}}{[[u]]_{t(e)}^{(i+1)}}\right)$$

$$(13)$$

where $\Delta\left(\cdot\right)$ denotes the increment. It is shown the return mapping algorithm ensures that the frictional slip criterion meets the Kuhn–Tucker load conditions $\dot{\lambda} > 0$ and $F = 0$.

Remarks Bathe and Chaudhary (1985), Simo et al. (1986), Perić and Owen (1992) and Weyler et al. (2012) proposed the penalty based frictional contact algorithms. In their work, the tangential displacement jump is divided into the elastic and plastic parts, and the positive normal and tangential penalty stiffnesses are used in the return mapping algorithm. However, these algorithms are not suitable for the cohesive/friction coupled problem because of tangential cohesive softening behavior. During numerical iterations in Eq. (13), the tangential elastic displacement jump $[[u]]_{t(e)}$ increases and the tangential traction T_t decreases, but the normal elastic displacement jump $\left|\left([[u]]_{n(e)}^{(i+1)}\right)\right|$ increases and the normal traction $|T_n|$ increases, which guarantees the convergence of the proposed algorithm at $|F| < tol\,(tol$ is the tolerance). In addition, it is noted the introduction of $\mu\,|T_n|$ helps to accelerate the convergence of the proposed algorithm in Eq. (13) because $\left|d_t^{(i+1)}\right|$

decreases and $\Delta\lambda$ increases and $|T_n|^{(i+1)}$ increases. Finally, the normal traction $T_n = T_n\left([[u]]_{n(e)}\right)$, the tangential traction $T_t = \mu_s\,|T_n|$ and the tangential stiffness $K_t = K_t\left([[u]]_{t(e)}\right)$ are updated after convergence.

Appendix 2: 3D finite element formulation for cohesive models

The node displacement $\boldsymbol{d}_N$ in the global coordinate system (1, 2, 3) is written as

$$\boldsymbol{d}_N = (d_x^1, d_y^1, d_z^1, d_x^2, d_y^2, d_z^2 \cdots d_x^8, d_y^8, d_z^8) \qquad (14)$$

The relative displacement between top and bottom surfaces is given by

$$\Delta\boldsymbol{u}_N = \boldsymbol{\phi}\boldsymbol{d}_N = \left(-\boldsymbol{I}_{12\times12}\ \boldsymbol{I}_{12\times12}\right)\boldsymbol{d}_N \qquad (15)$$

where $\boldsymbol{I}$ is the identity matrix and $\boldsymbol{\phi}$ is a 12×24 matrix.

The displacement at any point within the cohesive element in the global coordinate system (1, 2, 3) is calculated as

$$\Delta\boldsymbol{u}\left(\xi, \eta\right) = \begin{pmatrix} \Delta u_x\left(\xi, \eta\right) \\ \Delta u_y\left(\xi, \eta\right) \\ \Delta u_z\left(\xi, \eta\right) \end{pmatrix}$$
$$= \boldsymbol{H}\left(\xi, \eta\right)\Delta\boldsymbol{u}_N = \boldsymbol{H}\left(\xi, \eta\right)\boldsymbol{\phi}\boldsymbol{d}_N = \boldsymbol{B}\boldsymbol{d}_N \qquad (16)$$

where $\boldsymbol{H}\left(\xi, \eta\right)$ is the 3×12 shape function and $\boldsymbol{B}$ is the strain matrix.

The coordinate $\boldsymbol{x}_R^N$ at any reference surface in the deformed configuration is interpolated as

$$\boldsymbol{x}_R^N = \frac{1}{2}\left(\boldsymbol{I}_{12\times12}\ \boldsymbol{I}_{12\times12}\right)(\boldsymbol{x}_N + \boldsymbol{d}_N) \qquad (17)$$

where $\boldsymbol{x}_N$ is the initial node coordinate in the cohesive element.

The displacement jump $[[\boldsymbol{u}]]$ at any point in the cohesive element in the local coordinate system (ξ, η, ζ) is written as

$$[[\boldsymbol{u}]] = \boldsymbol{\Theta}^T\Delta\boldsymbol{u}(\xi, \eta), \quad \boldsymbol{\Theta} = (\boldsymbol{n}, \boldsymbol{t}_1, \boldsymbol{t}_2) \qquad (18)$$

where $\boldsymbol{\Theta}$ is the transformation matrix where three components are given by

$$\boldsymbol{n} = \frac{\left(\frac{\partial\boldsymbol{x}^R}{\partial\xi} \times \frac{\partial\boldsymbol{x}^R}{\partial\eta}\right)}{\left\|\frac{\partial\boldsymbol{x}^R}{\partial\xi} \times \frac{\partial\boldsymbol{x}^R}{\partial\eta}\right\|}, \quad \boldsymbol{t}_1 = \frac{\frac{\partial\boldsymbol{x}^R}{\partial\xi}}{\left\|\frac{\partial\boldsymbol{x}^R}{\partial\xi}\right\|}, \quad \boldsymbol{t}_2 = \boldsymbol{n} \times \boldsymbol{t}_1 \ (19)$$

where $\boldsymbol{x}^R = \boldsymbol{H}\left(\xi, \eta\right)\boldsymbol{x}_R^N$ is a point on the reference surface. $\boldsymbol{n}$ is the normal direction and $\boldsymbol{t}_1$ and $\boldsymbol{t}_2$ are the tangential directions.

Finally, the node residual force vector $\boldsymbol{f}_{24\times1}$ and the stiffness tensor $\boldsymbol{K}_{24\times24}$ of 3D cohesive elements are defined by

$$\boldsymbol{f}_{24\times1} = \int_{-1}^{1} \int_{-1}^{1} \boldsymbol{B}^T \boldsymbol{\Theta}^T \boldsymbol{T} \det J \mathrm{d}\xi \mathrm{d}\eta \tag{20}$$

$$\boldsymbol{K}_{24\times24} = \frac{\partial \boldsymbol{f}}{\partial \boldsymbol{d}_N} = \int_{-1}^{1} \int_{-1}^{1} \boldsymbol{B}^T \boldsymbol{\Theta}^T \boldsymbol{D}^s \boldsymbol{\Theta} \boldsymbol{B} \mathrm{d}\xi \mathrm{d}\eta$$

$$\boldsymbol{D}^s = \begin{bmatrix} K_n & \\ & K_t \end{bmatrix} \tag{21}$$

Appendix 3: Mode-II shear delamination fracture toughness of composites

Four methods for calculating the mode-II ERR are: 1 Compliance theory (Broek 1984), 2 Beam theory (Russell and Street 1982), 3 Modified beam theory (Carlsson et al. 1986) and 4 Associative beam theory and first-order shear deformation theory (Ozdil et al. 1998). The mode-II delamination fracture toughness G_{II}^c is determined using the initial delamination crack length $a = a_0$ and the corresponding experimental load value P(Theotokoglou and Vrettos 2006).

Compliance theory (Broek 1984)

Load-line compliance $C = \Delta/P$ is defined, where Δ is the displacement at the central loading point and P is the applied load. The ERR G_{II} takes the form

$$G_{\mathrm{II}} = \frac{P^2}{2b} \frac{\partial C}{\partial a} \tag{22}$$

where a is the actual crack length and b is the width of the specimen.

Beam theory (Russell and Street 1982)

The load-line compliance C_{BT} and the mode-II ERR G_{II}^{BT} are given by the beam theory

$$C_{\mathrm{BT}} = \frac{2L^3 + 3a^3}{8E_1 b h^3} \tag{23}$$

$$G_{\mathrm{II}}^{BT} = \frac{9a^2 P^2}{16E_1 b^2 h^3} \tag{24}$$

where E_1 is the longitudinal elastic modulus.

Modified beam theory (Carlsson et al. 1986)

Equations (25) and (26) were modified to include the effect of transverse shear deformation

$$C_{\mathrm{SH}} = C_{\mathrm{BT}} + \frac{1.2L + 0.9a}{4bG_{13}h} \tag{25}$$

$$G_{\mathrm{II}}^{\mathrm{SH}} = G_{\mathrm{II}}^{\mathrm{BT}} \left[1 + 0.2 \left(\frac{E_1}{G_{13}} \right) \left(\frac{h}{a} \right)^2 \right] \tag{26}$$

where G_{13} is the shear modulus.

Associated beam theory and first-order shear deformation theory (Ozdil et al. 1998)

By combining the laminate beam theory and the first order shear deformation theory, the compliance and the mode-II ERR are given by

$$C_{\mathrm{SBT}} = \frac{L^3 (d_{11})_{\mathrm{BC}}}{6b} + \frac{L(a_{55})_{\mathrm{BC}}}{2bk} + \frac{a^3 [(d_{11})_{\mathrm{AB}} - (d_{11})_{\mathrm{BC}}]}{12b} + \frac{a [(a_{55})_{\mathrm{AB}} - (a_{55})_{\mathrm{BC}}]}{4bk} \tag{27}$$

$$G_{\mathrm{II}}^{\mathrm{SBT}} = \frac{P^2}{8b^2} \left\{ a^2 [(d_{11})_{\mathrm{AB}} - (d_{11})_{\mathrm{BC}}] + \frac{(a_{55})_{\mathrm{AB}} - (a_{55})_{\mathrm{BC}}}{k} \right\} \tag{28}$$

where $k = 5/6$ is the shear correction factor, AB is the delaminated section, BC is a part of the intact section of the ENF specimen in Fig. 6, and $(d_{11})_{\mathrm{AB}}$, $(d_{11})_{\mathrm{BC}}$, $(a_{55})_{\mathrm{AB}}$ and $(a_{55})_{\mathrm{BC}}$ are the effective bending and shear compliances, respectively.

To calculate C_{SBT} and $G_{\mathrm{II}}^{\mathrm{SBT}}$ for the ENF specimen, the effective bending and shear compliances are calculated according to the method proposed by Ozdil et al. (1998).

Appendix 4: Analytical formulas for the load–displacement curves for mode-II delamination of ENF composites

According to the analytical formulas derived by Mi et al. (1998), the load–displacement curve of the ENF composite specimen is divided into three parts:

Curve $- \overline{\mathrm{OB}}: \quad \Delta = \frac{P(2L^3 + 3a_0^3)}{96E_1 I} \tag{29}$

Curve $- \overline{\mathrm{ABC}}(a < L):$

$$\Delta = \frac{P}{96E_1 I} \left[2L^3 + \frac{\left(64G_{\mathrm{II}}^c b E_1 I\right)^{3/2}}{\sqrt{3}P^3} \right] \tag{30}$$

Curve $- \overline{\mathrm{DE}}(a > L):$

$$\Delta = \frac{P}{24E_1 I} \left[2L^3 - \frac{\left(64G_{\mathrm{II}}^c b E_1 I\right)^{3/2}}{4\sqrt{3}P^3} \right] \tag{31}$$

where I is the second-order inertia moment and a_0 is the initial crack length.

References

Abdul-Baqi A, Van der Giessen E (2002) Numerical analysis of indentation-induced cracking of brittle coatings on ductile substrates. Int J Solids Struct 39:1427–1442

Alfano G, Crisfield M (2001) Finite element interface models for the delamination analysis of laminated composites: mechanical and computational issues. Int J Numer Methods Eng 50:1701–1736

Alfano G, Sacco E (2006) Combining interface damage and friction in a cohesive zone model. Int J Numer Methods Eng 68:542–582

Barenblatt GI (1962) The mathematical theory of equilibrium cracks in brittle fracture. Adv Appl Mech 7:55–129

Bathe KJ, Chaudhary A (1985) A solution method for planar and axisymmetric contact problems. Int J Numer Methods Eng 21:65–88

Bažant ZP, Oh BH (1983) Crack band theory for fracture of concrete. Mater Struct 16:155–177

Benzeggagh ML, Kenane M (1996) Measurement of mixed-mode delamination fracture toughness of unidirectional glass/epoxy composites with mixed-mode bending apparatus. Compos Sci Technol 56:439–449

Broek D (1984) Elementary engineering fracture mechanics, 3rd edn. Martinus Nijhoff Publishers, The Hague

Camacho G, Ortiz M (1996) Computational modelling of impact damage in brittle materials. Int J Solids Struct 33:2899–2938

Camanho PP, Davila C, De Moura M (2003) Numerical simulation of mixed-mode progressive delamination in composite materials. J Compos Mater 37:1415–1438

Campilho RDSG, Banea MD, Neto JABP, da Silva LFM (2013) Modelling adhesive joints with cohesive zone models effect of the cohesive law shape of the adhesive layer. Inter J Adhes Adhes 44:48–56

Carlsson L, Gillespie J, Pipes R (1986) On the analysis and design of the end notched flexure (ENF) specimen for mode II testing. J Compos Mater 20:594–604

Chaboche J, Girard R, Schaff A (1997) Numerical analysis of composite systems by using interphase/interface models. Comput Mech 20:3–11

Cheng L, Guo TF (2007) Void interaction and coalescence in polymeric materials. Int J Solids Struct 44:1787–1808

Dugdale DS (1960) Yielding of steel sheets containing slits. J Mech Phys Solids 8:100–104

Fan C, Ben Jar PY, Roger Cheng JJ (2007) A unified approach to quantify the role of friction in beam-type specimens for the measurement of mode II delamination resistance of fibre-reinforced polymers. Compos Sci Technol 67:989–995

Foulk J, Allen D, Helms K (2000) Formulation of a three-dimensional cohesive zone model for application to a finite element algorithm. Comput Methods Appl Mech Eng 183:51–66

Gao YF, Bower AF (2004) A simple technique for avoiding convergence problems in finite element simulations of crack nucleation and growth on cohesive interfaces. Model Simul Mater Sci Eng 12:453–463

Geubelle PH, Baylor JS (1998) Impact-induced delamination of composites: a 2D simulation. Compos Part B Eng 29:589–602

Goyal VK, Johnson ER, Davila CG (2004) Irreversible constitutive law for modeling the delamination process using interfacial surface discontinuities. Compos Struct 65:289–305

Guiamatsia I, Nguyen GD (2014) A thermodynamics-based cohesive model for interface debonding and friction. Int J Solids Struct 51:647–659

Gustafson PA, Waas AM (2009) The influence of adhesive constitutive parameters in cohesive zone finite element models of adhesively bonded joints. Int J Solids Struct 46:2201–2215

Harper PW, Hallett SR (2008) Cohesive zone length in numerical simulations of composite delamination. Eng Fract Mech 75:4774–4792

Hattiangadi A, Siegmund T (2005) An analysis of the delamination of an environmental protection coating under cyclic heat loads. Eur J Mech A/Solids 24:361–370

Jiang WG, Hallett SR, Green BG, Wisnom MR (2007) A concise interface constitutive law for analysis of delamination and splitting in composite materials and its application to scaled notched tensile specimens. Int J Numer Methods Eng 69:1982–1995

Krueger R (2004) Virtual crack closure technique: history, approach, and applications. Appl Mech Rev 57:109–143

Liljedahl CDM, Crocombe AD, Wahab MA, Ashcroft IA (2006) Damage modelling of adhesively bonded joints. Int J Fract 141:147–161

Lin G, Geubelle P, Sottos N (2001) Simulation of fiber debonding with friction in a model composite pushout test. Int J Solids Struct 38:8547–8562

Liu PF (2015) Extended finite element method for strong discontinuity analysis of strain localization of non-associative plasticity materials. Int J Solids Struct 72:174–189

Liu PF, Hou SJ, Chu JK, Hu XY, Zhou CL, Liu YL, Zheng JY, Zhao A, Yan L (2011) Finite element analysis of postbuckling and delamination of composite laminates using virtual crack closure technique. Compos Struct 93:1549–1560

Liu PF, Islam MM (2013) A nonlinear cohesive model for mixed-mode delamination of composite laminates. Compos Struct 106:47–56

Liu PF, Gu ZP, Peng XQ, Zheng JY (2015) Finite element analysis of the influence of cohesive law parameters on the multiple delamination behaviors of composites under compression. Compos Struct 131:975–986

Liu PF, Yang YH (2014) Finite element analysis of the competition between crack deflection and penetration of fiber-reinforced composites using virtual crack closure technique. Appl Compos Mater 21:759–771

Liu PF, Zheng JY (2013) On the through-the-width multiple delamination, and buckling and postbuckling behaviors of symmetric and unsymmetric composite laminates. Appl Compos Mater 20:1147–1160

Mi Y, Crisfield MA, Davies GA, Hellweg HB (1998) Progressive delamination using interface elements. J Compos Mater 32:1246–1272

McGarry JP, Máirtín ÉÓ, Parry G, Beltz GE (2014) Potential-based and non-potential-based cohesive zone formulations

under mixed-mode separation and over-closure. Part I: Theoretical analysis. J Mech Phys Solids 63:336–362

Moës N, Belytschko T (2002) Extended finite element method for cohesive crack growth. Eng Fract Mech 69:813–833

Mortensen F, Thomsen OT (2002) Analysis of adhesive bonded joints: a unified approach. Compos Sci Technol 62:1011–1031

Noorman DC (2014) Analysis on crack propagation in adhesives and adherends. Master thesis, Delft University of Technology

Ortiz M, Pandolfi A (1999) Finite-deformation irreversible cohesive elements for three-dimensional crack-propagation analysis. Int J Numer Methods Eng 44:1267–1282

Ozdil F, Carlsson L, Davies P (1998) Beam analysis of angle-ply laminate end-notched flexure specimens. Compos Sci Technol 58:1929–1938

Park K, Paulino GH, Roesler JR (2009) A unified potential-based cohesive model of mixed-mode fracture. J Mech Phys Solids 57:891–908

Parrinello F, Failla B, Borino G (2009) Cohesive-frictional interface constitutive model. Int J Solids Struct 46:2680–2692

Parrinello F, Marannano G, Borino G, Pasta A (2013) Frictional effect in mode II delamination: experimental test and numerical simulation. Eng Fract Mech 110:258–269

Perić D, Owen D (1992) Computational model for 3D contact problems with friction based on the penalty method. Int J Numer Methods Eng 35:1289–1309

Raous M, Cangémi L, Cocu M (1999) A consistent model coupling adhesion, friction, and unilateral contact. Comput Methods Appl Mech Eng 177:383–399

Russell A, Street K (1982) Factors affecting the interlaminar fracture energy of graphite/epoxy laminates. Progress in science and Engineering of Composites, ICCM-IV, Tokyo, Japan, pp 279–286

Rybicki EF, Kanninen MF (1977) A finite element calculation of stress intensity factors by a modified crack closure integral. Eng Fract Mech 9:931–938

Schellekens JCJ, de Borst R (1993) On the numerical integration of interface elements. Int J Numer Methods Eng 36:43–66

Schön J (2000) Coefficient of friction of composite delamination surfaces. Wear 237:77–89

Segurado J, LLorca J (2004) A new three-dimensional interface finite element to simulate fracture in composites. Int J Solids Struct 41:2977–2993

Serpieri R, Sacco E, Alfano G (2015) A thermodynamically consistent derivation of a frictional-damage cohesive-zone model with different mode I and mode II fracture energies. Eur J Mech A/Solids 49:13–25

Simo JC, Wriggers P, Schweizerhof K, Taylor R (1986) Finite deformation post-buckling analysis involving inelasticity and contact constraints. Int J Numer Methods Eng 23:779–800

Snozzi L, Molinari JF (2013) A cohesive element model for mixed mode loading with frictional contact capability. Int J Numer Methods Eng 93:510–526

Theotokoglou E, Vrettos C (2006) A finite element analysis of angle-ply laminate end-notched flexure specimens. Compos Struct 73:370–379

Turon A, Camanho PP, Costa J, Dávila C (2006) A damage model for the simulation of delamination in advanced composites under variable-mode loading. Mech Mater 38:1072–1089

Turon A, Davila CG, Camanho PP, Costa J (2007) An engineering solution for mesh size effects in the simulation of delamination using cohesive zone models. Eng Fract Mech 74:1665–1682

Tvergaard V (1990) Effect of fibre debonding in a whisker-reinforced metal. Mater Sci Eng A 125:203–213

Tvergaard V, Hutchinson JW (1993) The influence of plasticity on mixed mode interface toughness. J Mech Phys Solids 41:1119–1135

Van den Bosch M, Schreurs P, Geers M (2006) An improved description of the exponential Xu and Needleman cohesive zone law for mixed-mode decohesion. Eng Fract Mech 73:1220–1234

Weyler R, Oliver J, Sain T, Cante J (2012) On the contact domain method: a comparison of penalty and Lagrange multiplier implementations. Comput Methods Appl Mech Eng 205:68–82

Wisnom M, Jones M (1996) Measurement of friction in mode II delamination with through thickness compression. In: ECCM-7: seventh European conference on composite materials. Realising their commercial potential, pp 87–92

Wriggers P (2006) Computational contact mechanics, 2nd edn. Springer, Berlin

Xie D, Biggers SB Jr (2006) Progressive crack growth analysis using interface element based on the virtual crack closure technique. Finite Elem Anal Des 42:977–984

Xie D, Waas AM (2006) Discrete cohesive zone model for mixed-mode fracture using finite element analysis. Eng Fract Mech 73:1783–1796

Xu XP, Needleman A (1993) Void nucleation by inclusion debonding in a crystal matrix. Model Simul Mater Sci Eng 1:111–132

Xu YJ, Yuan H (2011) Applications of normal stress dominated cohesive zone models for mixed-mode crack simulation based on extended finite element methods. Eng Fract Mech 78:544–558

Yang QD, Cox B (2005) Cohesive models for damage evolution in laminated composites. Int J Fract 133:107–137

Yang QD, Thouless M, Ward S (1999) Numerical simulations of adhesively-bonded beams failing with extensive plastic deformation. J Mech Phys Solids 47:1337–1353